Doctoral Dissertation

Department of Advanced Materials Science
Graduate School of Frontier Sciences, The University of Tokyo

Structure and Dynamics of Connectivity -correlated Macromolecular Systems

2006

Satoshi Okabe

Contents

General Introduction

We are surrounded by many kinds of softmatters, such as polymers, liquid crystals, colloidal fluids, and so on. Many of them include solvents, which greatly affects physical properties of the systems through intermolecular interactions. One of the most interesting softmatter systems is gel. "Gel" is defined as a three dimensional network swollen by a great deal of solvent.[1] Gels have been widely studied in the last half century.[2–5] Most of these gels are polymer-based gels swollen in water, i.e., hydrogels. Since water is an excellent medium capable of various interactions, such as van der Waals interaction, hydrogen bonding, electrostatic interaction, and hydrophobic interaction, it is used as a common solvent for a variety of polymer-based gels. These interactions provide unique properties of polymer gels which are readily applied to industry, daily life, and medical application, etc., such as water absorbents, drug delivery systems, actuators, and sensors.[5] On the other hand, organogels, i.e., gels swollen in organic solvents, are also used as collectors of waste oil by solidification and as viscosity enhancers for foods and cosmetics.

In practice, gels are classified roughly to two categories, i.e., chemical gels and physical gels (Figure 1). The most popular way of preparing chemical gels is polymerization of a monomer solution in the presence of crosslinking agents. It is also possible to obtain chemical gels by ultraviolet or gamma-ray irradiation, which causes intermolecular recombination in polymer or monomer solutions.[6,7] On the other hand, physical gels are obtained by utilizing physical interactions between molecules in solvents. The physical interactions, such as hydrogen bonding, hydrophobic interaction, are capable of reversible intermolecular self-assembling, which causes frozen macromolecular structures resulting in fluidity lost. Gelatin and agar are typical gelling agents in aqueous systems, by which reversible physical gelations occur via hydrogen bonding by cooling after complete dissolution at high temperature. Physical gelation is thus a reversible reaction with respect to external stimuli, and it is easy to vary the

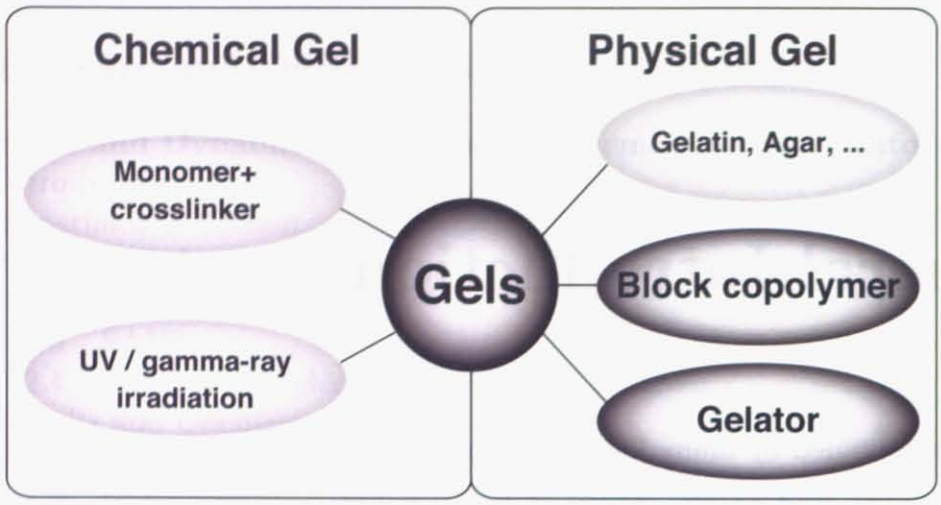

Figure 1: Chemical gels and physical gels with various preparation methods.

gelation criteria and physical properties of gels simply by choosing the combination of polymer and solvent. This is why physical gels are useful materials in industry and in daily life.

Recently, block copolymers and gelators gather much attention due to their abilities of gelation in water and/or organic solvents. As will be introduced in the following sections, these systems have potentiality of self-assembly by utilizing intermolecular interactions, such as hydrogen bonding and hydrophobic interaction. These interactions may cause strong "connectivity-correlation" between molecules, resulting in three-dimensional macromolecular networks formed by the associated molecules in solvents, i.e., physical gels.

There are many studies on physical gels with a view of structure, of course, but only a few studies treat gels as inhomogeneous and/or frozen matter. It is interesting to study whether they have the inherent nature of gels, such as non-ergodicity, frozen dynamics, etc. Here, the terms "non-eogodicity" and "frozen dynamics" respectively indicate inequality of statistics between ensemble- and time-averages, and a restricted cooperative motion.

The characteristic scales in these structure and phenomena range a wide spatio-temporal space (Figure 2), which can be well covered by small-angle neutron scattering (SANS) and dynamic light scattering (DLS) investigations. The space ranges nm to μm and the time range is ms to s. The obtained information could unveil the relationship among the chemical architectures, the resulting structures, dynamics,

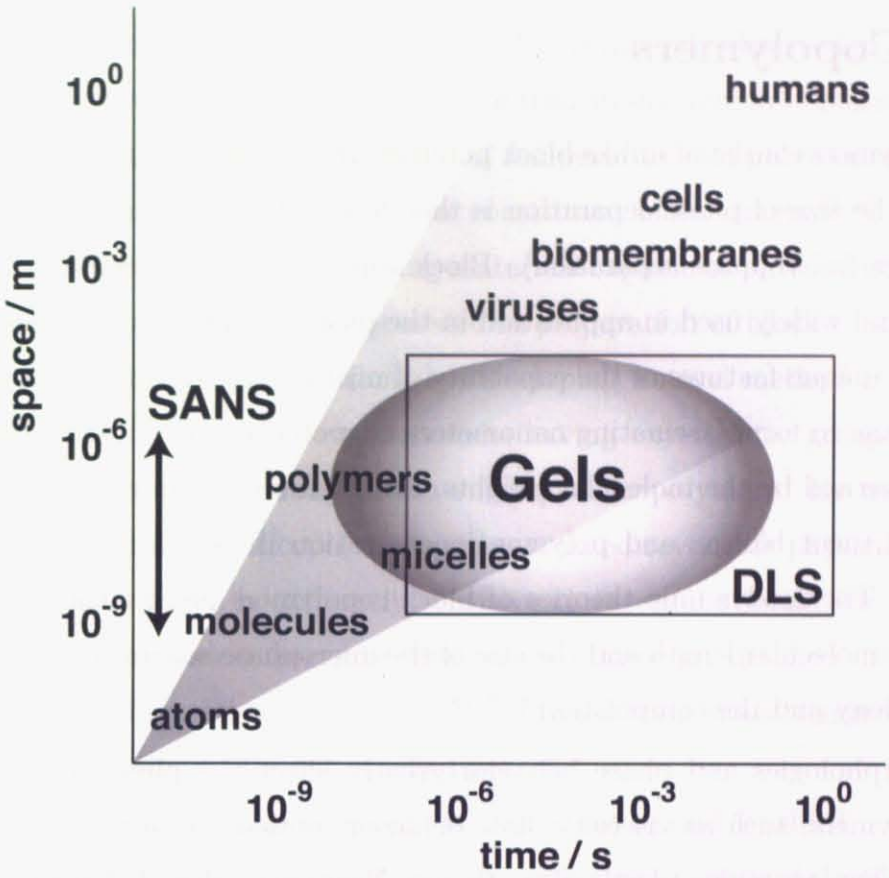

Figure 2: Spatio-temporal scales of "materials" and "life", and the regions covered by SANS and DLS.

and physical properties. Since gels lie at the junction of "materials" and "life", these studies may provide us a strategy of creating novel materials and of understanding life phenomena.

In the following sections, block copolymers and gelators are introduced briefly.

Block Copolymers

Block copolymers consist of unlike block polymer chains chemically connected to each other, and the size of phase separation is therefore restricted in order of the size of the polymers (microphase separation). Block copolymers have been extensively investigated and widely used in application in the past four decades.[8] This is partially due to their unique features of the capability of microphase separation, which causes self-assembling to form fascinating nanometer-order structures.[9–13] Microphase separation is governed by the molecular weights, composition, the interaction parameter of the constituent blocks, and polymer concentration if the block copolymer is in a solvent.[14] Thermodynamic theories of block copolymers predict the relationships between the molecular length and the size of the microphase separation, and between the morphology and the composition.[8,15–18]

The morphologies and phase behavior greatly affect the physical properties of block copolymers, such as viscosity, flow behavior, optical properties, and gas permeability. For example, plastic flow to non-Newtonian flow behavior transition and non-Newtonian to Newtonian flow behavior transition were observed for polystyrene-*block*-polybutadiene (PS-*b*-PB) in n-tetradecane (C14) when temperature was raised.[19–21] Here, C14 is a selective solvent for polybutadiene (PB) and a non-solvent for polystyrene (PS). Small-angle X-ray scattering studies revealed that these transitions are assigned to be lattice ordering and order-disorder transition, respectively. This is an analogy of solid-liquid-vapor phase transitions. In the "solid phase", PS-*b*-PB forms microphase separated structure with cubic packing of PS spherical domains. As temperature increases, "crystal" melting takes place to liquid phase, where the PS (non-soluble component) keeps its spherical domain structure as "micelles" with PB corona chains. This is followed by dissolution of PS micelles to a homogeneous polymer solution (liquid-to-vapor transition).

Similar structure transitions were also observed in aqueous solutions of polyethylene oxide-polypropylene oxide-polyethylene oxide (PEO-*b*-PPO-*b*-PEO) block copolymers. In this case, PEO-*b*-PPO-*b*-PEO chains are molecularly dispersed in water at low temperatures. When temperature was raised, PPO blocks form micelles with PEO corona. Further heating results in formation of crystalline lattice structure, i.e., "inverse crystallization". The inverse crystallization, meaning crystallization by heat-

ing, is due to hydrophobic nature of PPO which is commonly observed in hydrophobic polymers in aqueous solutions. The structure transitions were systematically studied by Mortensen by using SANS as functions of temperature and polymer concentration in addition to of molecular weights of the constituent block chains.[22–24]

Block copolymers are thus promising materials capable of physical gelation in solutions. Recently, Aoshima et al. succeeded in preparation of block copolymers with narrow molecular weight distributions by developing a novel method of living polymerization. This method employs monomers having oxyethylene groups in the side chain, leading to water-solubility of the subsequent copolymers. By utilizing these "quasi-monodisperse" block copolymers, they realized reversible physical gelation in aqueous solutions, which is extremely sensitive to external stimuli, such as temperature, solvent composition, pressure, and so on. However, detailed mechanisms of gelation, such as sharp sol-to-gel transition, sol-to-gel transitions triggered by various kinds of external stimuli, are not clarified yet.

Living polymerization also allows one to choose the second (or third, ...) monomers to be attached on during polymerization. This provides a variety of chemical architectures for copolymers, such as graft, random, and star-shaped copolymers. Gradient copolymer has a concentration gradient along the polymer chain. It is of interest to explore the microscopic behavior of gradient copolymers because an introduction of a concentration gradient to a polymer chain may exhibit novel properties.

Gelators

In comparison with hydrogels, development of organogels have been faced several difficulties because a variety of organic solvents, such as alcohols, hydrocarbons, aromatic solvents, ketones, amines, silicon oils, mineral oils, etc., have been taken into account. The first criterion for a gelator is that the gelator is soluble in the targeting solvent. The second criterion is that the gelator is capable of self-organization to form a supramolecular network. This is necessary to immobilize the solvent with an infinite network of the gelator by its self-assembling.

Hanabusa et al. prepared various types of gelators, such as boraform amides derived from amino acids.[25–28] They found that amino acid derivatives are suitable of candidates of gelators. On the other hand, Beginn et al. synthesized a series of gelators on the basis of different concepts.[29–33] According to them, a simple rational concept to construct gel forming molecules is to prepare nearly flat amphiphilic molecules consisting of small polar and bulky non polar parts. Dastidar and coworkers proposed another type of gelator, which is an organic salt of bile acids and amines.[34] They employed a combinatorial method to explore high-performance gelators and obtained an ambidextrous gel displaying the ability to form gels with organic as well as aqueous solvents.

In any case, it is important to bestow a functional group capable of hydrogen bond formation and long alkyl groups. The former is necessary for self-assembling and the latter for increasing solubility to the organic solvent. Up to date, what we have learned are the following. The basic requirements for a gelator are presence of (1) functional groups capable of intermolecular association, (2) lipophilic groups for dissolution, and (3) bulky and/or asymmetric group for anti-crystallization. A large number of gelators, which meet the above requirements, have been reported.[35,36] However, the gelators made for practical use have been limited. This is partially because studies on the structure-property relationship of organogelators have been still limited.[35] It is important to clarify the relationship between molecular architecture and the associated structure in order to develop a designing concept for novel types of gelators.

Outline of the Dissertation

By considering the above situations, I intended to investigate the relationship among molecular architectures, microscopic structures, and dynamics of the connectivity-correlated systems including block copolymer and gelator systems. The following is the lineup of the contents of this dissertation.

Part I: Improvement of the SANS Technique

Experimental studies require the reliability of measurements and data analyses, and instrumentation is therefore positioned as an important task in this dissertation. In this part, the instrumental setup and a novel theory for small-angle neutron scattering experiments are described.

The SANS-U is a 32 m-small-angle neutron scattering (SANS) instrument, owned by the Institute for Solid State Physics, the University of Tokyo, installed in 1991 at the guide hall of the JRR-3M research reactor of the Japan Atomic Energy Agency, Tokai, which has been served as an inter-university cooperative research use since 1993. In order to expand the applicable conditions of experiments and to improve the reliability, a major upgrade was made by replacement of the area detector, the control system, and refurbishment of the cables, mechanical systems, electronic systems, etc. Details of the upgrade and the performance of the new SANS-U are described in **Chapter 1**.

In addition to the instrumental issue, evaluation of incoherent neutron scattering is important especially for softmatter systems. One of the major components of softmatter systems is hydrogen, which is the element containing the largest incoherent scattering cross-section. The structure information is obtained from the coherent scattering, whereas the incoherent scattering provides a scattering-angle-independent background. This is why an incoherent scattering subtraction is an inevitable process in SANS data analyses. In **Chapter 2**, a novel method for evaluation for incoherent small-angle neutron scattering from softmatters in a parallel-plate shape is proposed by properly taking account of the multiple scattering effect.

Part II: Structure and Dynamics in Block Copolymer Solutions

In **Chapter 3**, the sharp and thermoreversible morphological transitions in aqueous solutions of poly(2-ethoxyethyl vinyl ether)-*block*-poly(2-hydroxyethyl vinyl ether) (EOVE-*b*-HOVE)) showing interesting physical properties, such as an extremely sharp sol-to-gel transition during heating process are discussed. This transition takes place in a narrow temperature window less than a degree of centigrade and the elastic modulus of the system increases by the factor of more than 10^4. The origin of this sharp transition is investigated from the viewpoint of microscopic structure and thermal property.

In **Chapter 4**, the dynamic aspects of thermoreversible morphological transition of EOVE-*b*-HOVE in aqueous solutions are investigated by DLS and rheological measurements. A sample-position dependent DLS study is also employed in order to elucidate the detailed transition mechanism, such as molecular dispersion-to-micelle transition and micelle-to-macrolattice transition, which cannot be sufficiently resolved by SANS. Rheological behavior, i.e., Newtonian-to-non-Newtonian transition and non-Newtonian-to-plastic flow transition, are explained systematically by the structural transitions.

In **Chapter 5**, the microphase separation of solvent-sensitive self-assembling block copolymer, poly(2-phenoxyethyl vinyl ether)-*block*-poly(2-methoxyethyl vinyl ether) (PhOVE-*b*-MOVE), in acetone/water mixture is investigated by SANS. Acetone solutions of PhOVE-*b*-MOVE undergo tremendous viscosity thickening by adding small amount of water, which will be explained by the structural transition indicated by the SANS experiments. A contrast variation SANS experiment also allows us to elucidate the micelle architecture consisting of gathered polyPhOVE domains with tethered polyMOVE chains spread in the matrix. The structure evolution of this "water-induced microphase separation" was compared with that of previously discussed "heat-induced microphase separation".

In **Chapter 6**, structural investigations are carried out on aqueous solutions of block (Block) and gradient copolymers (Grad) comprising EOVE and MOVE, where MOVE denotes 2-methoxyethyl vinyl ether. Here, Grad has a monomer-composition gradient along the polymer chain. Although aqueous solutions of EOVE homopoly-

mer precipitated at 20 °C, the two copolymer systems showed different temperature dependence. A 0.3 wt% of Grad system had a micellization temperature range between 20 and 30 °C, while Block system underwent a sharp transition at around 20 °C. The micellization mechanisms and resulting micelle sizes in the Block and Grad systems are investigated by DLS and SANS, and the characteristic behavior in Grad system is explained by a novel concept, i.e., the reel-in phenomenon.

In **Chapter 7**, a SANS investigation is carried out on semi-dilute solutions of Block and Grad in order to elucidate viscoelastic transition mechanisms and the relationship between structure and mechanical property. In 20 wt% solutions, a microphase-separated structure and physical gelation are observed both for Block and for Grad systems. By comparing the structural parameters, such as micelle size, scattering contrast factor, and their temperature dependence between the Block and Grad systems, the role of the "reel-in" process in the microphase separation is explained.

Part III: Structure and Dynamics in Gelator Systems

In **Chapter 8**, SANS and light scattering (LS) studies are carried out on an organogel consisting of a gelator, coded P-1, and dimethylsulfoxide (DMSO). The gelator P-1 is made of an oligosiloxane stem and about 8 branches of an amino acid derivative combined with a long alkyl chain. The amino acid part, *N*-n-pentanoyl-*L*-isoleucylaminooctadecane, is responsible for intermolecular association via hydrogen bonding between amide groups. After complete dissolution of P-1 in DMSO at 85 °C, the solution is cooled down to obtain a physical gel. During the gelation process, the variation of scattered light intensity is monitored as a function of temperature in order to determine the gelation threshold. The SANS results unveil the structure in this organogel. The gelation mechanism is proposed in view of the resulting structure and gel dynamics.

In **Chapter 9**, SANS and DLS investigation are carried out for organogels in toluene formed by various types of gelators in order to elucidate the relationship between the chemical structure and the gelation mechanism as well as the physical properties of the resulting gels. Three different types of gelators, i.e., cyclo(*L*-β-3,7-

dimethyloctylasparaginyl-*L*-phenylalanyl) (CPA), trans-(1*R*,2*R*)-bis(undecylcarbonylamino)cyclohexane (TCH), and N^{ε}-lauroyl-N^{α}-stearylaminocarbonyl-*L*-lysine ethyl ester (LEE), are chosen for comparison. Here, the characteristic features of the gelation properties, such as the critical gelation concentration, C_{gel}, the gelation temperature, T_{gel}, the gel structure, and the gelation mechanism, are different from each other. CPA had the lowest C_{gel} and became a gel gradually as temperature decreased, while TCH and LEE had higher C_{gel} and underwent a sharp sol-gel transition. The relationship between mechanism of physical gelation and chemical architecture is investigated.

References

[1] Osada, Y.; Kajiwara, K. *Gel Handbook*; Academic Press, N.Y., 2001.

[2] Stockmayer, W.H. *J. Chem. Phys.* 1943, **11**, 45.

[3] Flory, P. J. *Principles of Polymer Chemistry*; Cornell Univ. Press, Ithaca, N.Y., 1953.

[4] Tanaka, T. *Sci. Am.* 1981, **224**, 110.

[5] Rossi, D; Kajiwara, K.; Osada, Y.; Yamauchi, A. *Polymer Gels*; Plenum Press, N.Y., 1991.

[6] Ikkai, F.; Adachi, E. *Macromol. Rapid Commun.* 2004, **25**, 1514.

[7] Kishi, R.; Hirasa, O.; Ichijo, H. *Polym. Gels Netw.* 1997, **5**, 145.

[8] Hamley, I. W. *The Physics of Block Copolymers*; Oxford University Press: Oxford, 1998.

[9] Zhang, L.; Eisenberg, A. *Science* 1995, **268**, 1728.

[10] McConnell, G. A.; Gast, A. P. *Macromolecules* 1997, **30**, 435.

[11] McConnell, G. A.; Gast, A. P.; Huang, J. S.; Smith, S. D. *Phys. Rev. Lett.* 1993, **71**, 2102.

[12] Alexandridis, P.; Ollson, U.; Lindman, B. *Langmuir* 1998, **14**, 2627.

[13] Molau, G. E. In S. L. Aggarwal Ed.; *Block Polymers*; Plenum Press: N.Y., 1970.

[14] Shibayama, M.; Hashimoto, T.; Kawai, H. *Macromolecules* 1983, **16**, 1093.

[15] Helfand, E.; Wasserman, Z. R. *Macromolecules* 1976, **9**, 879.

[16] Helfand, E.; Wasserman, Z. R. In I. Goodman Ed.; *Developments in Block Copolymers*; Applied Science: N.Y., 1982.

[17] Helfand, E.; Wasserman, Z. R. *Macromolecules* 1978, **11**, 960.

[18] Leibler, L. *Macromolecules* 1980, **13**, 1602.

[19] Watanabe, H.; Kotaka, T.; Hashimoto, T.; Shibayama, M.; Kawai, H. *J. Rheology* 1982, **26**, 153.

[20] Shibayama, M.; Hashimoto, T.; Kawai, H. *Macomolecules* 1983, **16**, 16.

[21] Hashimoto, T.; Shibayama, M.; Kawai, H.; Watanabe, H.; Kotaka, T. *Macomolecules* 1983, **16**, 361.

[22] Mortensen, K. *Progress in Colloid and Polym. Sci.* 1993, **93**, 72.

[23] Mortensen, K. *Progress in Colloid and Polym. Sci.* 1993, **91**, 69.

[24] Mortensen, K.; Brown, W. *Macromolecules* 1993, **26**, 4128.

[25] Hanabusa, K.; Tanaka, R.; Suzuki, M.; Kimura, M.; Shirai, H. *Adv. Mater.* 1997, **9**.

[26] Hanabusa, K.; Tange, J.; Taguchi, Y.; Koyama, T.; Shirai, H. *Chem. Commun.* 1993, 390.

[27] Hanabusa, K.; Hiratsuka, K.; Kimura, M.; Shirai, H. *Chem. Mater.* 1999, **11**, 649.

[28] Hanabusa, K.; Kobayashi, H.; Suzuki, M.; Kimura, M.; Shirai, H. *Colloid. Polym. Sci.* 1998, **276**, 252.

[29] Beginn, U.; Keinath, S.; Moeller, M. *Macromol. Chem. Phys.* 1998, **199**, 2379.

[30] Beginn, U.; Sheiko, S.; Moeller, M. *Macromol. Chem. Phys.* 2000, **201**, 1008.

[31] Beginn, U.; Tartsch, B. *Chem. Commun.* 2001, 1924.

[32] Beginn, U.; Zipp, G.; Moeller, M. *J. Polym. Sci.: Part A: Polym. Chem.* 2000, **38**, 631.

[33] Beginn, U.; Zipp, G.; Moeller, M. *Adv. Mater.* 2000, **12**, 510.

[34] Dastidar, P.; Okabe, S.; Nakano, K.; Iida, K.; Miyata, M.; Thonai, N.; Shibayama, M. *Chem. Mater.* 2005, **17**, 741-748.

[35] Terech, P.; Weiss, R. G. *Chem. Rev.* 1997, **97**, 3133.

[36] Hanabusa, K. In *Macromolecular Nanostructured Materials*; Ueyama, N.; Harada, A., Eds.; Springer-Verlag: Berlin, 2005, p 118-137.

Part I

Improvement of the SANS Technique

Chapter 1

Upgrade of a 32m Small-angle Neutron Scattering Instrument, SANS-U

1.1 Introduction

Small-angle neutron scattering (SANS) is a unique and non-destructive method for structural analyses in many fields, such as biological and polymeric systems, colloidal suspensions, membranes, flux lines in superconductors, etc. The structural information obtained by SANS covers the spatial range of a few to hundred nanometer and have been revealing important scientific findings for more than three decades.[1,2] Because of the above usefulness, a large number of steady reactor-sourced SANS instruments have been constructed and served for users, e.g., D11 (1972 -) and D22 (1995 -) at ILL (France), NG1, NG3 (1992 -), and NG7 (1991 -) at NIST (U.S.),[3] SANS-J at JAEA (Tokai, Japan), and SANS-U at ISSP (Tokai, Japan),[4] etc., in addition to pulsed neutron-sourced instruments, such as, LOQ at ISIS (U.K.),[5] SASI & SAND at IPNS (U.S.), LQD at LANSCE (U.S.), SWAN at KEK (Tsukuba, Japan).[6] New powerful SANS instruments are under construction at ORNL (U.S.), HANARO (Korea), ANSTO (Australia), etc.

The SANS-U, owned by the Institute for Solid State Physics, The University of Tokyo, was constructed in the guide hall of the 20 MW research reactor, JRR-3M, of the Japan Atomic Energy Agency in 1991.[4] Figure 1.1 shows the overview of SANS-U. This instrument is 32m long and is composed of (a) a mechanical neutron velocity selector (NVS), (b) a pre-sample flight path, (c) a multi purpose sample stage, (d) an evacuated post-sample flight path, (e) an area detector, (f) a point

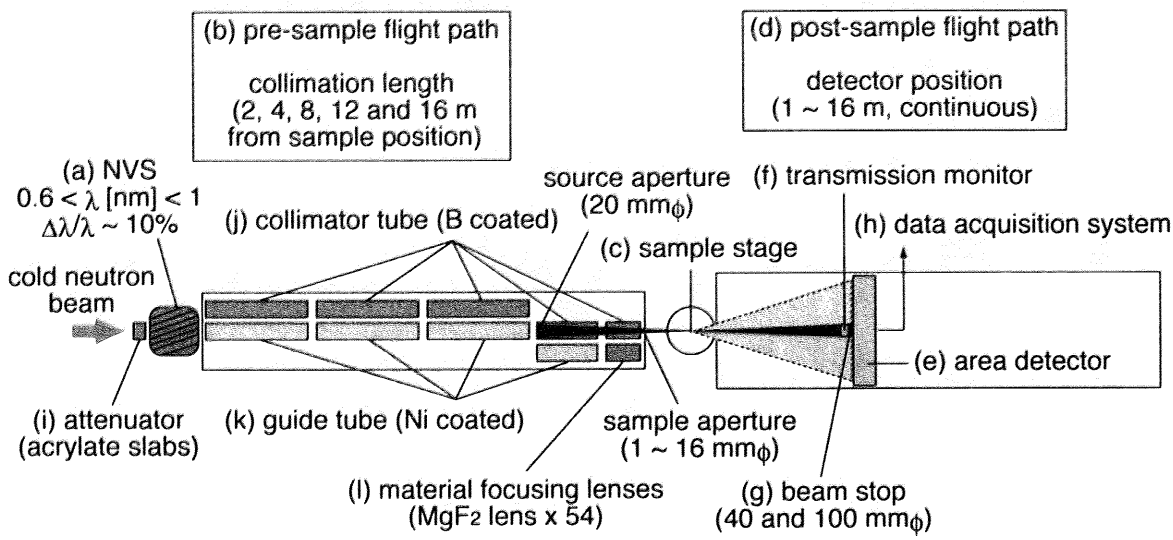

Figure 1.1: The overview of the SANS-U.

detector for transmission measurements, (g) a beam stop made of B_4C, and (h) a data acquisition system. The incident neutron beam from the cold source (white beam flux $\sim 2 \times 10^8$ $cm^{-2}s^{-1}$ with the peak wavelength of 0.4 nm) is monochromatized by a NVS with helical slits (ASTRIUM, Germany).[7] Cold neutron beam from the reactor was guided to the NVS. If necessary, the beam can be attenuated by (i) polyacrylate slabs with different thicknesses (3, 5, and 7 mm). Just behind the NVS is located the pre-sample flight path, which consists of (j) pinhole tubes coated with B_4C inside and (k) alternate neutron guide tubes coated with Ni inside. By replacing the pinholes and the guide tubes in or out of the beam, users can change the effective source-to-sample distance (= collimation length, CL) to 1, 2, 4, 8, 12, or 16 m in order to vary the divergence and flux of the incident beam at the sample position. Normally, a symmetric optical arrangement, i.e., CL = SDD (sample-to-detector distance), is recommended to optimize the flux and divergence of the beam. The collimator apertures are 20 mmϕ each and the sample aperture can be chosen from 1, 3, 5, 7, 8, 10 to 16 mmϕ. (l) A set of material focusing lenses,[8,9] made of 54 pieces of MgF_2 biconcave lenses, can be inserted at the lower-most collimator tube position for converging optics. The focal length is 8.0 m for $\lambda = 0.70$ nm. The unique feature of the symmetric arrangement will be discussed later. For higher resolution experiments, CL is set to be longer than SDD. The sample stage is designed to be versatile for various types of sample systems. In the past decade, various types of

sample systems such as a high-pressure cell, a furnace, a shear cell, etc., have been developed by users and the Instrumentation and Research Team (IRT). Scattered neutrons are fed by an evacuated flight path, in which an area detector of 64.5 cm × 64.5 cm is installed on a truck running on rails to vary the SDD continuously from 1 m to 16 m. A slide-in type direct beam stop and beam monitor for measurements of transmission are mounted on the truck just in front of the detector.

However, due to chronic insufficiency of beam time, aging of the electronics and cables, and out-of dating of the computer systems, an upgrade of SANS-U had been highly demanded. In order to expand the applicable conditions of experiments and to improve the reliability, a major upgrade has been made. The major upgrades of the SANS-U are (1) a replacement of the two-dimensional area detector from a single-wire type position-sensitive proportional counter to a multi-wire type, (2) a renewal of the operating system from a VAX and sequencers to an integrated PXI system controlled by LabVIEW-RT software, (3) a focusing collimation system, and (4) a variety of accessory equipments, such as furnace, high pressure cell, shear cell, in addition to a versatile sample changer. The lineup of the above devices and the performance of the new SANS-U are described.

1.2 Upgrade of SANS-U

1.2.1 Replacement of the area detector

The two-dimensional area detector, which was a single-wired position sensitive proportional counter (PSPC; model 2650N, ORDELA, USA), was replaced by a multi-wired PSPC (model 2660N, ORDELA, USA). Because of the multi-wired cathodes for both the horizontal (X) and vertical (Y) directions and of a lower ^{3}He gas pressure, the maximum count rate was raised from 10^5 to 10^6 cps/detector (catalogue base). For safety use, we regulate the upper limit of counting rate to be 7000 cps/detector and 200 cps/pixel. The data acquisition system (DAS100) was also supplied by ORDELA, which is an integrated board developed for data accumulation and detector configurations.

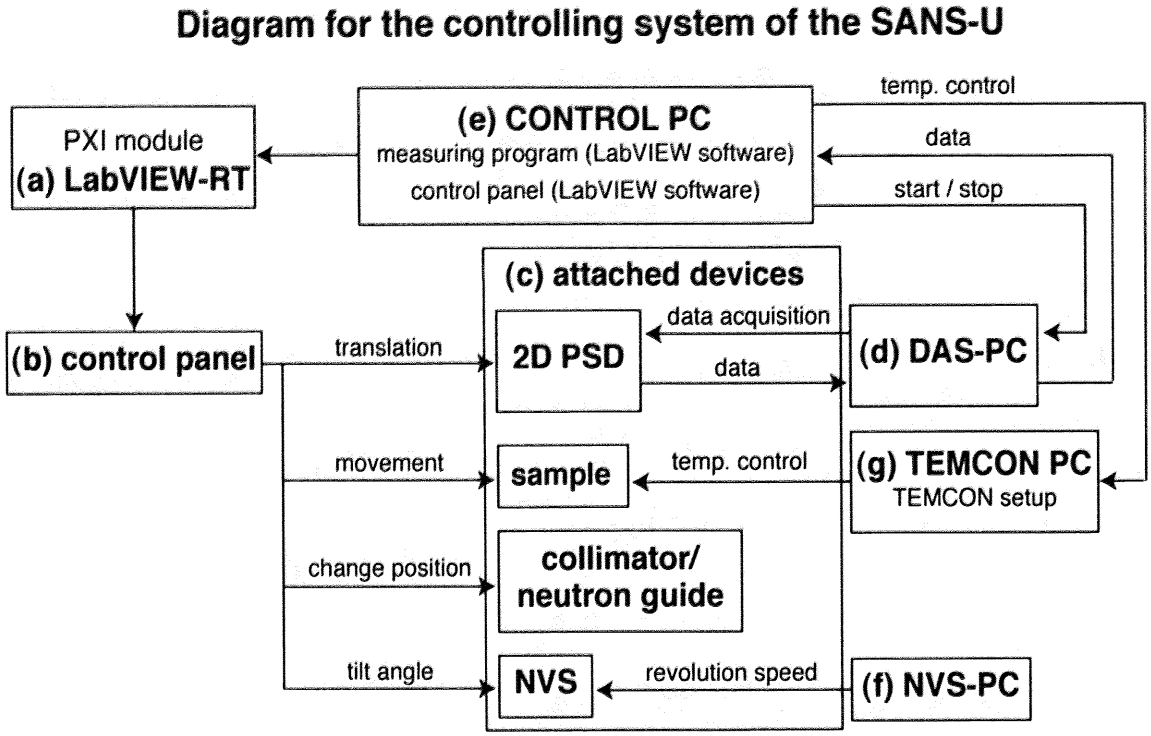

Figure 1.2: Diagram of the SANS-U control system.

1.2.2 Replacement of the SANS-U control system

The previous SANS-U control system ran on a VAX with a set of sequencers. The experimental conditions were set by way of isolated sequencers. By upgrading, the SANS-U control system was replaced by a LabVIEW-RT system running on a PXI (PCI eXtensions for Instrumentation) system. The new SANS-U control system contains five WINDOWS and one Macintosh computers, the control panel, and the peripheral devices. Figure 1.2 shows the diagram of the relationship between the devices and the control system. (a) The LabVIEW-RT is an operating system, which has good compatibility with LabVIEW applications and guarantees a long-run stability. The main liquid-crystal display of the SANS-U control system has a mirror image of (b) the control panel, which allows a remote control of the experiment from the computer. All of the commands, such as change of collimation, sample change, goniometer control, temperature control, can be sent to (c) the peripheral devices. The scattering intensity data collected by the area detector was transferred to (d) the DAS-PC, followed by (e) the control PC. The NVS is controlled by (f) NVS-PC. A temperature control device (TEMCON) is operated by (g) TEMCON-PC.[10] Since

the SANS-U control program is written in LabVIEW, the system is very versatile and provides an amenity operation.

1.2.3 Real time circular/sectorial averaging

The LabVIEW environment also realizes easy integration of data acquisition and primitive analyses. The control system installed at the SANS-U contains a real time circular averaging function, which converts an original two-dimensional scattering intensity pattern to a circularly averaged one-dimensional profile. By simply typing the center channel of the profile and the rate of re-flushing, users are able to watch the evolution of the scattering profile during measurement. The resulting one-dimensional data and the original two-dimensional data are stored automatically to the control PC. Users are allowed to transfer the data to their own computers any time. This function has drastically improved operating efficiency as well as capability of designing the experiment *in situ*.

1.2.4 Accessories

A 500 mmϕ diameter sample stage is located between the pre- and post-sample flight paths. A variety of sample systems can be mounted on this stage, such as an automatic sample changer, an inner cell-type high-pressure cell (HP cell), a shear cell with a thermometer covering the range of shear rate from 10^{-3} to 10^{3} s^{-1},[11] a furnace for high temperature up to 250 °C, and a cryostat with electromagnets. The sample changer has horizontally-aligned 10 sample holders and the sample position can be changed automatically. The chamber is designed to tolerate evacuation for the use of high ($\leq$ 200 °C) and low ($\geq$ 10 °C) temperatures by either electric heater or water circulation. The HP cell has recently been designed to carry out high-pressure experiments for polymer solution or microemulsion systems. The accessible pressure is 400 MPa. Some experimental results have already been published.[12–14] Though it is under establishment, the details of the HP cell will be reported elsewhere in the near future. The sample stage can be rotated for fine adjustment of the sample systems to the optic axis and especially for θ-scan of solid-state crystals. Except for the shear cell system, the temperature of the sample can be controlled precisely by using TEMCON system[10] with an accuracy of less than 0.01 °C.

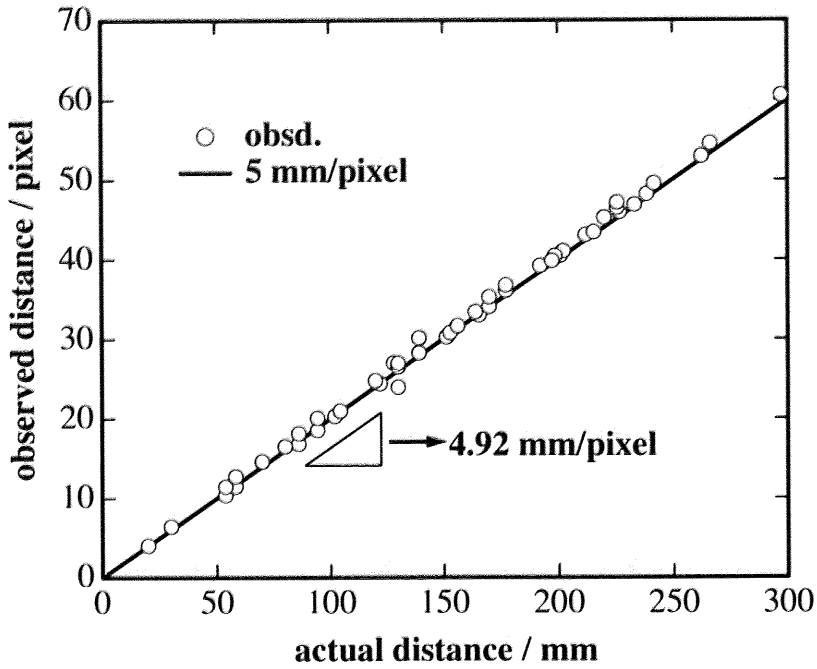

Figure 1.3: The spatial linearity of the area detector of SANS-U.

1.3 Calibration and Performance

1.3.1 Linearity of the detector

The linearity of the detector was measured by carrying out SANS measurement of a polyethylene (PE) slab. Here, just in front of the detector was placed a cadmium plate with 3 mm diameter holes aligned 5 cm interval orthogonally. Figure 1.3 shows the observed distances (in pixel) of the apertures from the center channel of the detector against the actual distances (in mm) from the center of the detector plane. This clearly indicates that the positions of the apertures are detected properly, meaning good linearity of the detector with 1 pixel = 4.92 mm.

1.3.2 Uniformity of the detector

The uniformity of the efficiency of the detector was measured by using incoherent scattering from H_2O in a quartz cell with the optical length of 2 mm. The scattering profile of H_2O was corrected for transmission, parasitic scattering from the cell and the dark current (Figure 1.4). The accumulated counts were 200 to 400 neutrons/pixels, resulting in 4×10^4 neutrons along the x- or y-directions. As shown in

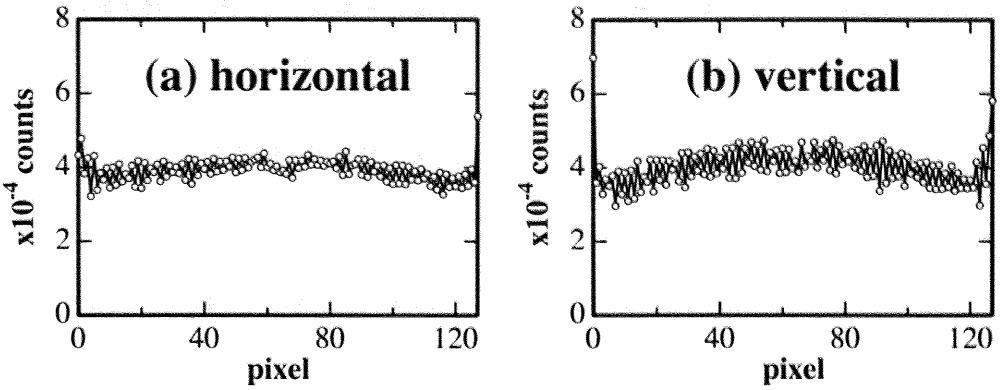

Figure 1.4: Performance test of the detector uniformity. (a) Horizontally (x-axis) and (b) vertically (y-axis) integrated incoherent scattering profiles from a polyethylene standard sample.

the figure, there are two types of inhomogeneities, i.e., odd-even type and gradient type inhomogeneities. Hence, currently a pixel-to-pixel correction for each data point is employed by using incoherent scattering from a polyethylene secondary standard.

1.3.3 Center beam profile

Figure 1.5 shows the geometrical scheme of the symmetric optical arrangement for the cases of CL = SDD = 4 (dashed lines) and 8 m (solid lines). A 5 mmϕ sample aperture is also set in the beam line. As shown in the figure, the incident beam profile on the detector plane is uniquely determined independent of CL (and SDD). The full width at half maximum (FWHM) is calculated to be 4 pixels (= 19.7 mm) when a 5 mmϕ sample aperture is used. The center beam profile along the x-axis at the optics of SDD = CL = 4 m with λ = 0.70 nm is shown in Figure 1.6a. A similar profile was obtained for the y-axis. The profile is nicely reproduced by a Gaussian function with FWHM of 3.45 pixels (= 17.3 mm), which is in good agreement with the evaluated value from Fig. 1.5. The FWHMs of the profile at other optical conditions are shown in Figure 1.6b. The value of FWHM increases with SDD up to 4m. This is due to the fact that CL was set to be constant, i.e., CL = 4 m, irrespective of SDD. On the other hand, a symmetrical optical condition was taken for the case with SDD $\geq$ 4 m.

The neutron flux at the sample plane is 6.0×10^5 cm^{-2} sec^{-1}, in the case of CL = 4 m. The incident beam intensity at the detector plane, $I^0_{\rm det}$, was measured by

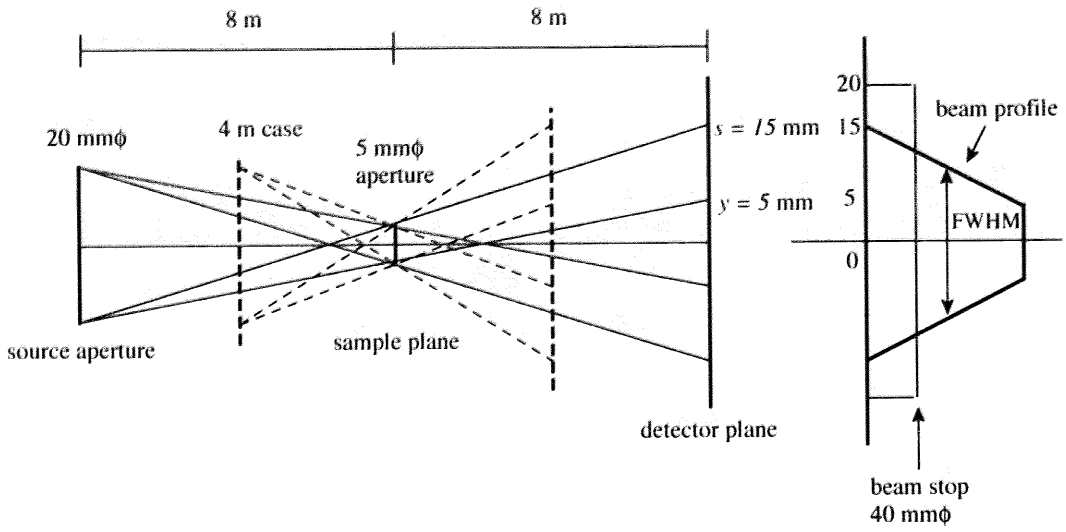

Figure 1.5: The geometrical scheme of the symmetric arrangement of SANS-U for SDD = 8 (solid lines) and 4 m (dashed lines).

using incoherent scattering from H_2 as shown in Figure 1.7 It was found that $I^0_{\rm det}$ was a function of SDD with a power of 1.91, $I^0_{\rm det} \propto {\rm SDD}^{-1.91}$ for the collimation-fixed optical conditions. The power ca. -2 is explained by the reduction of the solid angle covered by the detector plane with SDD. When the symmetric optical arrangement is applied (SDD = CL), the relationship became $I^0_{\rm det} \propto {\rm SDD}^{-3.92}$. The additional power -2 with respect to the collimation-fixed case is due to the reduction of the effective source area determined by the end of the neutron guide with CL.

1.3.4 Wavelength calibration

The wavelength calibration is carried out using Bragg reflections from a microphase separated block copolymer film (poly(styrene-d_8)-poly(isoprene), sample code : DI33) at the beginning of each reactor cycle. Two-dimensional scattering patterns containing sharp peaks are obtained as a function of the NVS revolution speed, $v_{\rm NVS}$. A sector averaging with the angle of 10 °is carried out to obtain a scattering function shown in Figure 1.8. By using an assumed wavelength, $\lambda_{\rm assum}$, the q-value of the first peak position, $q_{\rm assum}$, is determined by curve fitting of the peak profile with a Gaussian function. Here, q is the magnitude of the scattering vector defined by $q = (4\pi/\lambda)\sin\theta$, where 2θ is the scattering angle and λ is the wavelength of the incident neutron beam. The Bragg spacing of the DI33, d, is known to be $d = 44.5$

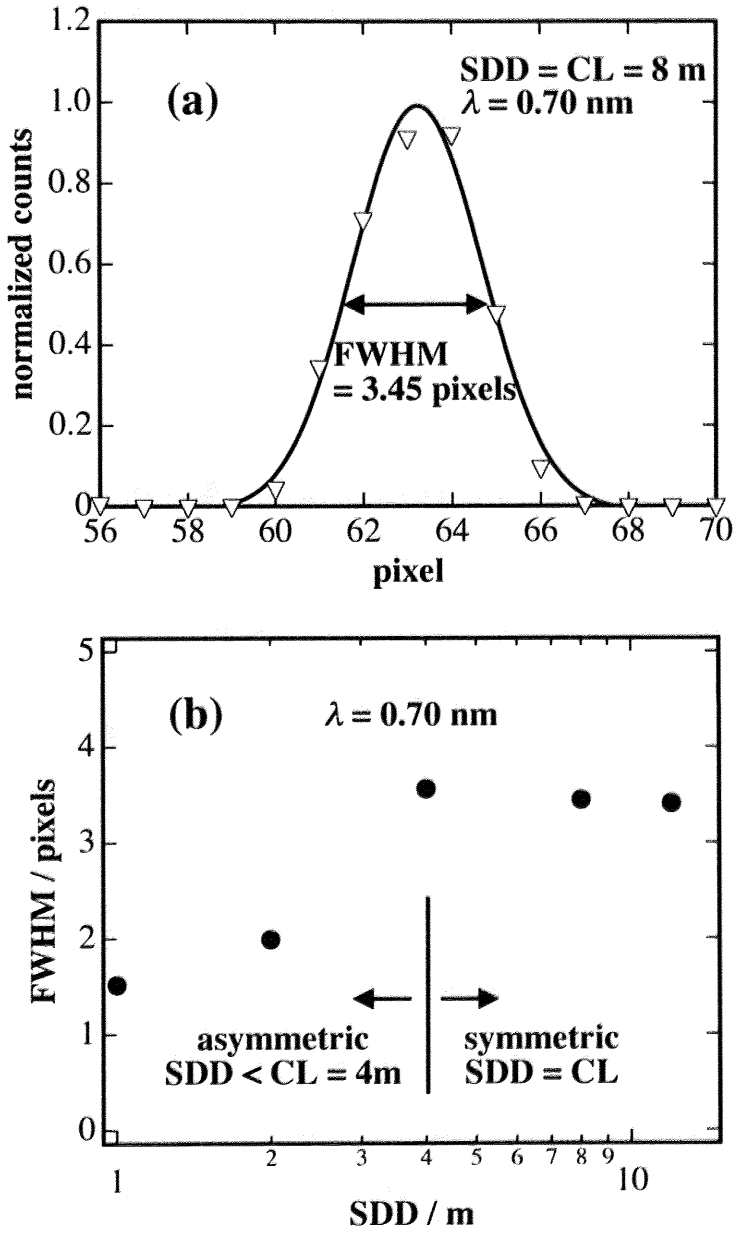

Figure 1.6: (a) The center beam profile along the x-axis at SDD = CL = 8 m. (b) The SDD dependence of FWHM of the divergence of the center beam.

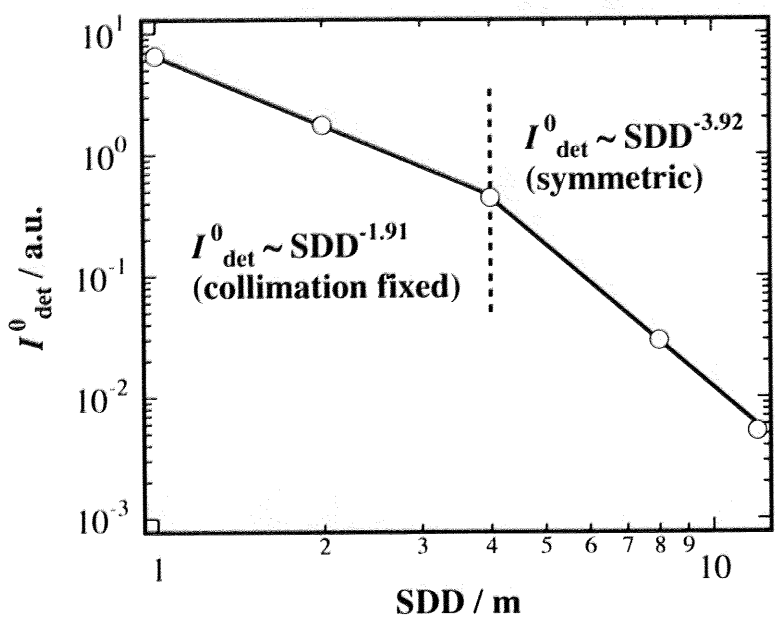

Figure 1.7: The incoherent scattering intensity from H_2O as as function of SDD and CL.

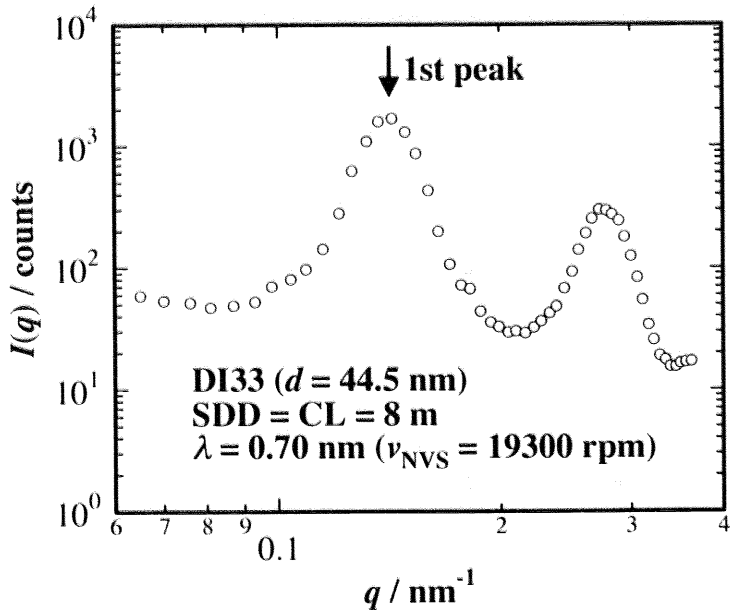

Figure 1.8: The scattering intensity function from DI33 used for wavelength calibration. (SDD = CL = 8 m.)

nm determined by small-angle X-ray scattering.[15] So the real wavelength, λ_{real}, can be obtained with the following equations.

$$q_{\mathrm{assum}}\lambda_{\mathrm{assum}} = q_{\mathrm{real}}\lambda_{\mathrm{real}} = \frac{2\pi}{d}\lambda_{\mathrm{real}} \tag{1.1}$$

Usually, λ is selected to be 0.70 nm after iterating the above procedure at several v_{NVS} values by assuming a linear relationship between v_{NVS} and λ. Figure 1.9a shows the plot of the wavelength, λ, as a function of the v_{NVS}. As shown in the figure, the relationship is rather linear in this region. Figure 1.9b shows the λ dependence of the incident beam intensity, which is a monotonically decreasing function of λ. From practical point of view, the wavelength $\lambda = 0.70$ nm is recommended by setting v_{NVS} around 1.9×10^4 rpm, which optimizes the flux and the q-resolution. The adjustable λ is $0.65 < q\ [\mathrm{nm}^{-1}] < 1.1$. The wavelength distribution is 10 % (FWHM) according to the manual of the NVS.[7]

1.3.5 Accessible q-range

The accessible q-range was evaluated by measuring incoherent scattering from Lupolen at various optical conditions. The scattering profiles are shown in Figure 1.10 for the cases of (a) CL = 4 m, SDD = 1 m, (b) CL = 4 m, SDD = 2 m, (c) CL = 4 m, SDD = 4 m, (d) CL = 8 m, SDD = 8 m, and (e) CL = 12 m, SDD = 12 m. The valid q-range was evaluated from the flat range of the scattering intensity in the figure. At $q \leq 0.16\ \mathrm{nm}^{-1}$, a slight upturn due to the concentration fluctuation of polyethylene is observed. However, it does not affect to the accessible q-range of the spectrometer. For example, when SDD = 4 m and CL = 4 m with $\lambda = 0.70$ nm, the accessible q-range is $0.08 < q\ [\mathrm{nm}^{-1}] < 0.8$. Hence, by choosing suitable set of different optical conditions, SANS-U covers a wide q-range of $0.04 < q\ [\mathrm{nm}^{-1}] < 3.5$ in the case of $\lambda = 0.70$ nm.

1.3.6 Focusing collimation

The performance of the focusing collimation with the material lenses was examined. In the upgraded SANS-U, a beam guide with 54 biconcave lenses can be mounted by remote control from the SANS-U control panel. Here, the specification of the lens is as follows; the curvature radius = 25.0 mm, the center thickness = 1.00 mm, and the outer diameter = 30.0 mm. In the case of SDD = 8 m symmetric optical arrangement

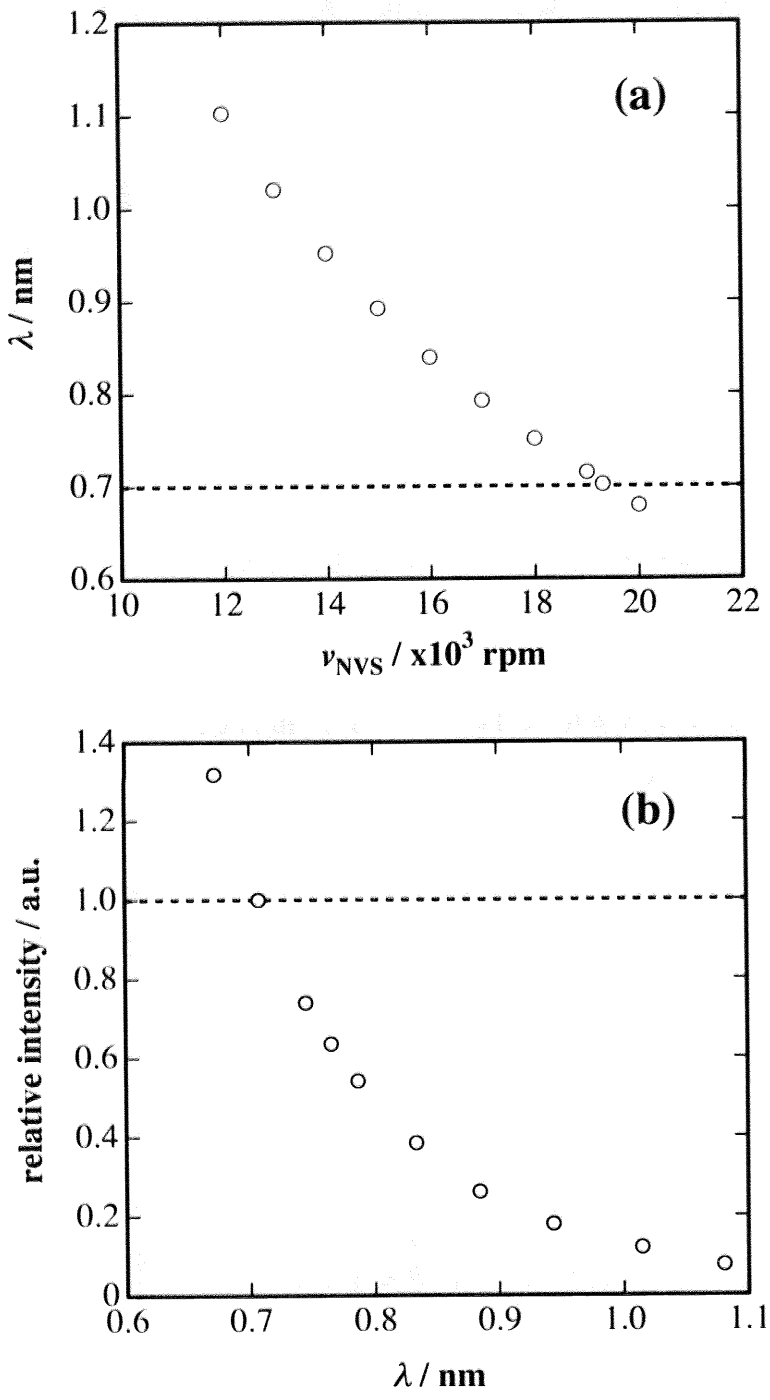

Figure 1.9: (a) The NVS revolution speed, ν_{NVS}, dependence of the wavelength, λ, and (b) the λ-dependence of the relative incident beam intensity normalized at $\lambda = 0.7$ nm.

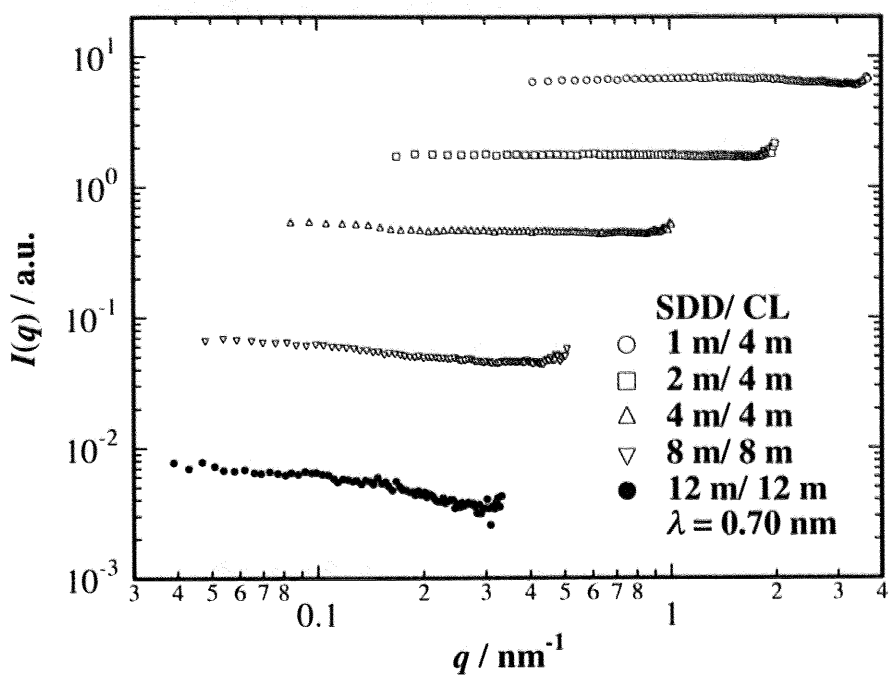

Figure 1.10: Background corrected scattering profiles of a polyethylene slab (3 mm thick), indicating the accessible q-ranges at various optical conditions.

with 20 mmϕ sample aperture, the transmittance of a $\lambda = 0.7$ nm neutron beam was 0.51 and the focal spot size on the detector plane was calculated to be 9.5 mm in diameter. Figure 1.11 shows the comparisons of the incident beam profiles at the detector plane with and without the focusing collimation system for the beam sizes of (a) 5 mmϕ and (b) 16 mmϕ. By enlarging the sample aperture, both the peak intensity and the sharpness of the profile was improved by the factors of 1.4 and 1.3 times, respectively. Hence, it is recommended to employ this setup if a large sample is available.

1.4 Data treatment at the SANS-U

1.4.1 Absolute intensity calibration

One of the greatest advantages of the SANS technique is that the absolute scattering intensity is easily obtained by scaling the observed scattering intensity with a standard sample, e.g., a vanadium standard or water. Since the zero-q scattering intensity, $I(q = 0)$, contains useful information such as molecular weight of polymers

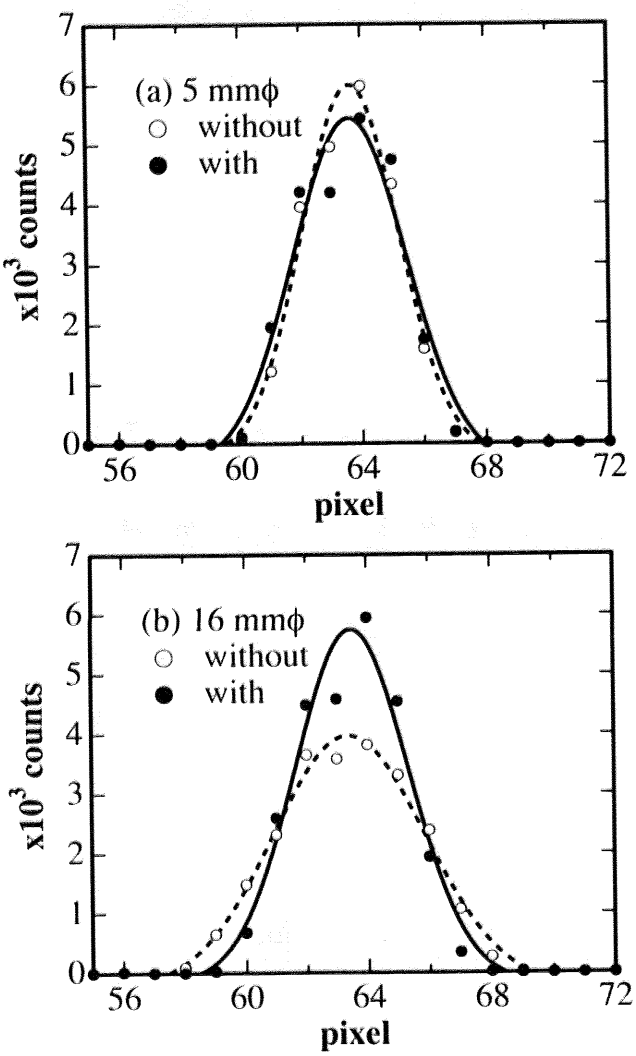

Figure 1.11: The center beam profiles with (filled symbols with solid line) and without the focusing collimation (open symbols with dashed line) system. (a) 5 mm and (b) 16mm sample apertures in diameter.

and the association number of particles, it is recommended to obtain the absolute scattering intensity at SANS-U as well as at other SANS instruments. Because of weak scattering and difficulty in handling of vanadium, vanadium-calibrated materials are used as the secondary standard samples. The secondary standard for absolute intensity calibration is Lupolen (polyethylene (PE) slab) at SANS-U. The following fact should be noted here. A PE slab with known mass density is more suitable as a standard than water since the latter contains larger inelastic scattering.[16] The effect of multiple scattering from PE slabs has been properly taken into consideration.[17] A calibrations for PEs was carried out by scaling the incoherent scattering intensity with that from the primary standard, vanadium.

In the case of single scattering, the normalized scattering intensity, $\mu(q)$ [-] is expressed by the following equation.[18]

$$\mu_{\mathrm{i}}(q) \equiv \frac{I_{\mathrm{i}}(q)}{\Phi_0 \varepsilon A \Delta\Omega} = T_{\mathrm{i}} t_{\mathrm{i}} \left(\frac{\mathrm{d}\Sigma}{\mathrm{d}\Omega}\right)_{\mathrm{i}} (q) \tag{1.2}$$

where $I_{\mathrm{i}}(q)$ [s^{-1}], T_{i}[$-$], and t_{i}[cm] are the corrected scattering intensity, the transmission for neutrons, and the thickness of i (i = L, V or S for Lupolen, vanadium or another sample). Φ_0[$\mathrm{cm}^{-2}s^{-1}$] is the flux of the incident beam, ε[$-$] is the efficiency of the detector, A[cm^2] is the irradiated cross section of the sample, $\Delta\Omega$[sr] is the solid angle at the detector plane. $I_{\mathrm{i}}(q)$[s^{-1}] is given by

$$I_{\mathrm{i}}(q) = \frac{\left[I^0_{\mathrm{i}}(q) - I^0_{\mathrm{bg}}(q)\right] - T_{\mathrm{i}}\left[I^0_{\mathrm{c}}(q) - I^0_{\mathrm{bg}}(q)\right]}{\cos^3 2\theta} \tag{1.3}$$

where $I^0_{\mathrm{i}}(q)$ [s^{-1}] is the count rate of the scattered neutrons from the sample (in a cell), $I^0_{\mathrm{bg}}(q)$[s^{-1}] is the detector dark current, $I^0_{\mathrm{c}}(q)$[s^{-1}] is the air scattering (or the scattering from the sample cell). The factor $1/\cos^3 2\theta$ corresponds to the correction for the oblique incidence and the q-dependence of the solid angle necessary for high-q region. By employing an identical optical condition for each measurement, i.e., the sample and the standard, we obtain a simple equation,

$$\mu_{\mathrm{PE}} = T_{\mathrm{V}} t_{\mathrm{V}} \left(\frac{\mathrm{d}\Sigma}{\mathrm{d}\Omega}\right)_{\mathrm{V}} \frac{I_{\mathrm{PE,inc}}}{I_{\mathrm{V,inc}}} \tag{1.4}$$

where T_{V} and t_{V} are the transmission and the thickness of the vanadium, and $I_{\mathrm{PE,inc}}$ and $I_{\mathrm{V,inc}}$ are the corrected scattering intensities of Lupolen and the vanadium. Note that $I_{\mathrm{PE,inc}}$, $I_{\mathrm{V,inc}}$ and therefore μ_{PE} are q-independent because both Lupolen and the

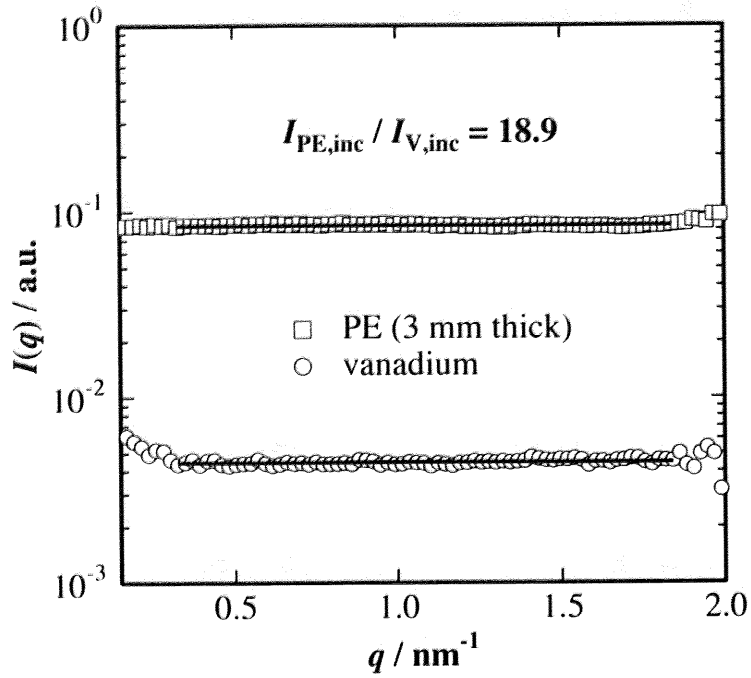

Figure 1.12: Comparison of the incoherent scattering intensities from vanadium and a polyethylene slab (3 mm in thick).

vanadium show incoherent scattering in small-angle region. The differential scattering cross section of vanadium, $(\mathrm{d}\Sigma/\mathrm{d}\Omega)_\mathrm{V}$, is estimated with the following equation,

$$\left(\frac{\mathrm{d}\Sigma}{\mathrm{d}\Omega}\right)_\mathrm{V} = \frac{\rho_\mathrm{V}\sigma_\mathrm{V,inc}}{4\pi} \tag{1.5}$$

where $\sigma_\mathrm{V,inc}$ is the incoherent scattering cross section, $\rho_\mathrm{V} = d_\mathrm{V}N_\mathrm{A}/M_\mathrm{V}$ and d_V are the number and the mass density, N_A is Avogadro's number and M_V is the molecular mass of vanadium. These values are well known from literatures as $\sigma_\mathrm{V,inc} = 5.08 \times 10^{-24}\mathrm{cm}^2, d_\mathrm{V} = 5.8\ \mathrm{gcm}^{-3}, M_\mathrm{V} = 50.94$. Therefore, $(\mathrm{d}\Sigma/\mathrm{d}\Omega)_\mathrm{V} = 0.0278\ \mathrm{cm}^{-1}$.

The corrected profiles, $I_\mathrm{PE,inc}$ and $I_\mathrm{V,inc}$ are shown in Figure 1.12. The ratio $I_\mathrm{PE,inc}/I_\mathrm{V,inc}$ was evaluated to be 18.9. By substituting this value and the values T_V and t_V, $\mu_\mathrm{PE} = 7.45 \times 10^{-2}$ was obtained from eq. 1.3. Note that μ_PE is sample thickness-dependent due to multiple scattering.

In practice, the differential scattering cross section of a sample, $(\mathrm{d}\Sigma/\mathrm{d}\Omega)_\mathrm{S}(q)$, is obtained by the following equation.

$$\left(\frac{\mathrm{d}\Sigma}{\mathrm{d}\Omega}\right)_\mathrm{S}(q) = \frac{I_\mathrm{S}(q)}{I_\mathrm{L,inc}}\frac{\mu_\mathrm{PE}}{T_\mathrm{S}t_\mathrm{S}} \tag{1.6}$$

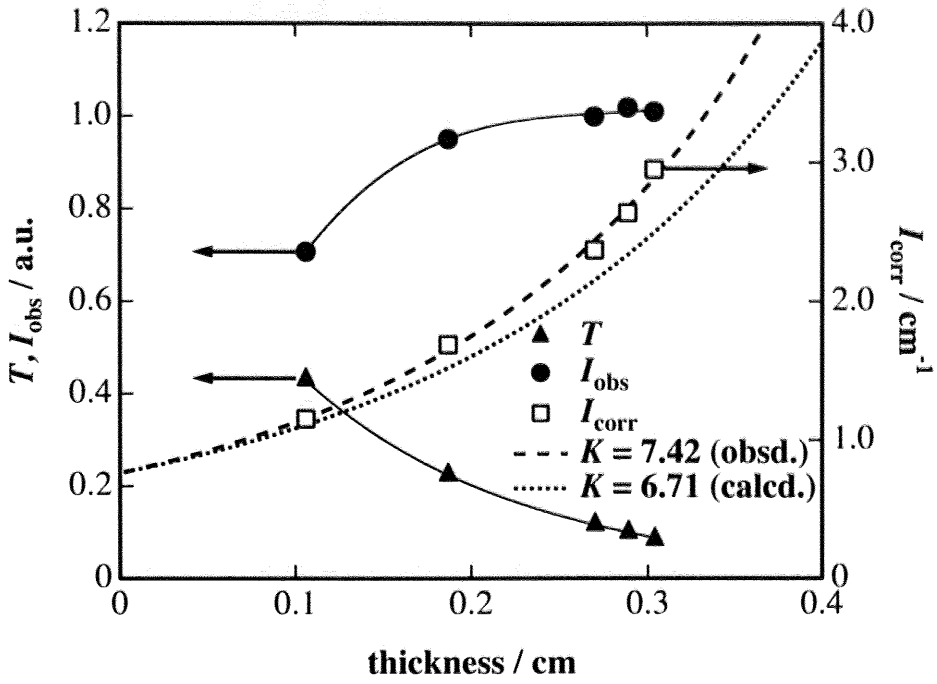

Figure 1.13: The thickness-dependence of the observed scattering intensity, transmission, and the corrected scattering intensity of PEs. The dotted and dashed lines indicate the theory and fitting result, respectively. The solid lines are guides for the eye.

1.4.2 Thickness dependence of incoherent scattering

Let us discuss the thickness dependence of the scattering intensity from polyethylene slabs. Figure 1.13 shows the thickness, t [cm], dependence of the observed scattering intensity, $I_{\rm obs}$, transmission, T, and the scattering intensity corrected with Eq. 1.6, $I_{\rm corr}$. As clearly shown, T is a monotonically decreasing function of t, obeying the Lambert-Beer's law,

$$T = \exp(-\mu t), \tag{1.7}$$

with $\mu = 7.99$ cm^{-1} which is close to that obtained previously.[17] On the other hand, the behaviours of $I_{\rm obs}$ and $I_{\rm corr}$ are rather complicated. These behaviours are mainly due to the multiple scattering as discussed elsewhere.[17] The observed $I_{\rm corr}$ is well reproduced by that expected theoretically in the following equation (dashed lines in Fig. 1.13).

$$I_{\rm corr} = I_{0,\rm corr} C \tag{1.8}$$

$$I_{0,\rm corr} = \frac{K}{4\pi} = \frac{\rho \sigma_{\rm s}}{4\pi} \tag{1.9}$$

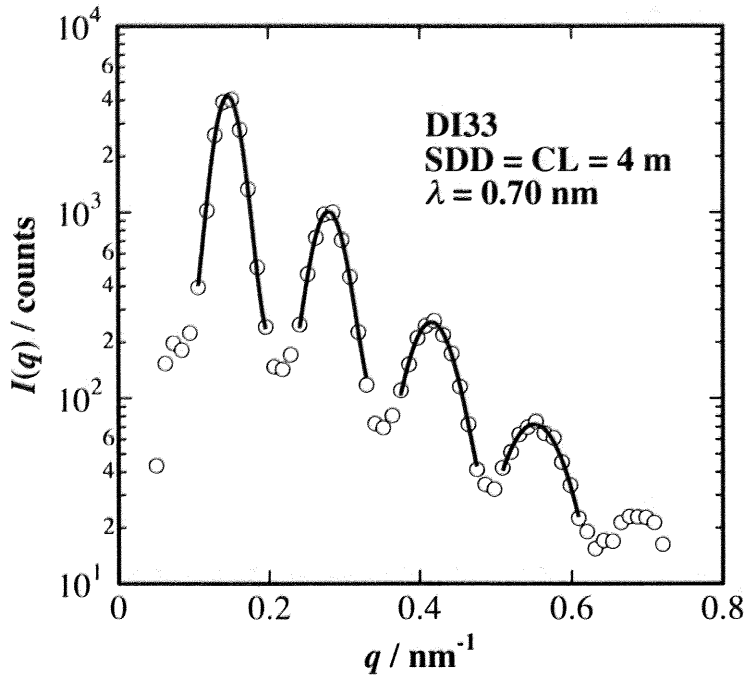

Figure 1.14: The scattering intensity from DI33. The solid lines indicate the fits of the scattering peaks with Gaussian functions, which allow an estimation of a decay of q-resolution with q.

$$\sigma_s = \sigma_{coh} + \sigma_{inc} \tag{1.10}$$

$$C = \frac{e^{Kt} - 1}{Kt} \tag{1.11}$$

Here, σ_{coh} and σ_{inc} are the coherent and incoherent scattering cross-sections, respectively. The factor $K = 7.42$ cm^{-1} obtained by curve fitting is close enough to 6.71 cm^{-1}, the calculated value for PE with the density of 0.922 gcm^{-3}.[17]

1.4.3 q-resolution

Next, let us discuss the q-resolution of this instrument. The q-resolution was evaluated with the sharpness of the Bragg reflections from the DI33 sample with SDD = CL = 4 m and $\lambda = 0.70$ nm (Figure 1.14). The relative peak positions obey the lamellar stacking, i.e., 1:2:3:... The square of FWHM of the peaks, δq^2, is plotted against q (Figure 1.15). It is clearly shown that FWHM becomes larger with increasing q. Smearing occurs by the following contributions; (i) an aperture smearing due to a finite size of the incident beam, (ii) the wavelength distribution of the incident neutrons, and (iii) the paracrystal nature of the microdomains in block copolymers.[20]

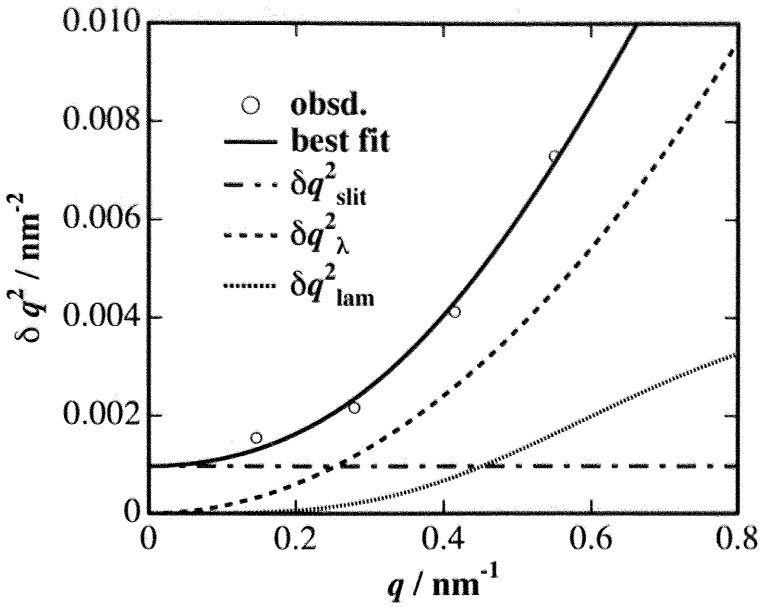

Figure 1.15: The q-dependence of FWHMs of the Bragg reflections from DI33.

The instrumental smearing, $\delta q_{\rm inst}$, is obtained by the sum of (i) and (ii), and is evaluated by

$$q = \frac{4\pi}{\lambda}\sin\theta \approx \frac{4\pi}{\lambda}\theta \text{ (when small-angle)} \tag{1.12}$$

$$\delta q^2_{\rm inst} = \delta q^2_{\lambda} + \delta q^2_{\rm apert} \tag{1.13}$$

$$\delta q^2_{\lambda} = \left|\frac{\partial q}{\partial \lambda}\delta\lambda\right| = \left|-\frac{4\pi}{\lambda^2}\sin\theta\delta\lambda\right| = \left|-q\frac{\delta\lambda}{\lambda}\right| \propto q^2 \tag{1.14}$$

$$\delta q^2_{\rm apert} = \left|\frac{\partial q}{\partial \theta}\delta\theta\right| \tag{1.15}$$

where the wavelength $\lambda = 0.70$ nm and its resolution $\delta\lambda/\lambda = 0.10$ (FWHM). The contribution (i) can be estimated from the optical arrangement. From Figure 1.6, the square of FWHM of the center beam profile at the detector plane, $\delta q^2_{\rm apert}$, was evaluated to be $1.60\times10^{-3}{\rm nm}^{-2}$. $\delta q^2_{\rm apert}$ is also evaluated by the following equation,[3,19]

$$\delta q^2_{\rm apert} = \frac{8\ln 2(2\pi)^2}{12\lambda^2}\left[3\frac{R_1^2}{L_1^2} + 3\frac{R_2^2}{L'^2} + \frac{(\Delta R)^2}{L_2^2}\right] \tag{1.16}$$

where R_1 and R_2 are the radii of the source and sample apertures, ΔR is the detector resolution (FWHM), and L_1 and L_2 are the incident and scattered flight path lengths, and L' is the reduced path length, $L' = L_1L_2/(L_1 + L_2)$, respectively. According to eq. (1.15), on the other hand, δq^2_{λ} is proportional to q^2, meaning that the q-resolution

Table 1.1: Comparison between values for the q-resolution function from the experiment, calculation and the fitting. (a) From the center beam profile on the detector, (b) (Mildner, 1984; Glinka, 1998), (c) From the catalogue from the manufacturer, (d) (Shibayama, 1986)

	exp.	calc.	fit
$\Delta q_{\text{apert}}[\text{nm}^{-2}]$	$0.00160^{(a)}$	$0.000763^{(b)}$	0.000967
$\Delta\lambda/\lambda$(FWHM)	n/a	$0.1^{(c)}$	0.123
g	$0.05^{(d)}$	n/a	0.0559

becomes worse by increasing q. In order to estimate the smearing effect of paracrystal nature of the sample, δq^2_{lam}, the paracrystal theory was adopted.[20,21] The theory gives

$$\delta q^2_{\text{lam}} = \frac{4\ln 2}{\pi}\frac{\{1-\exp[-2\pi^2 g^2 (q/q_1)^2]\}^2}{4q_1^2} \tag{1.17}$$

where g is the Hosemann's g-factor, q_1 the first peak position of Bragg reflection, and d the Bragg spacing of the lamellar structure. Thus the square of the total FWHM of the scattering peaks for the paracrystal system is

$$\begin{aligned}\delta q^2 &= \delta q^2_{\text{apert}} + \delta q^2_{\lambda} + \delta q^2_{\text{lam}} \\ &= \delta q^2_{\text{apert}} + \left(\frac{\delta\lambda}{\lambda}\right)^2 q^2 \\ &+ \frac{4\ln 2}{\pi}\frac{\{1-\exp[-2\pi^2 g^2 (q/q_1)^2]\}^2}{4q_1^2}\end{aligned} \tag{1.18}$$

Curve fitting was carried out on the plot of δq^2 vs q by floating parameters $\delta q^2_{\text{apert}}$, $\delta\lambda/\lambda$, and g. The fitted values are in good agreement with those obtained with other methods (Table 1) and we can conclude that the instrumental smearing effect in high q region is dominated by the λ-distribution.

1.4.4 Experimental Example

In order to demonstrate the performance of SANS-U, the molecular weight of a standard polystyrene (PS, the number and weight average molecular weights being $M_n = 2.08 \times 10^4$ and $M_w = 2.22 \times 10^4$, respectively, the polydispersity index = 1.07; Polymer Source Inc., Doval, Montreal, Canada) was evaluated. Deuterated cyclohexane solutions of the PS were prepared, and SANS experiments were carried

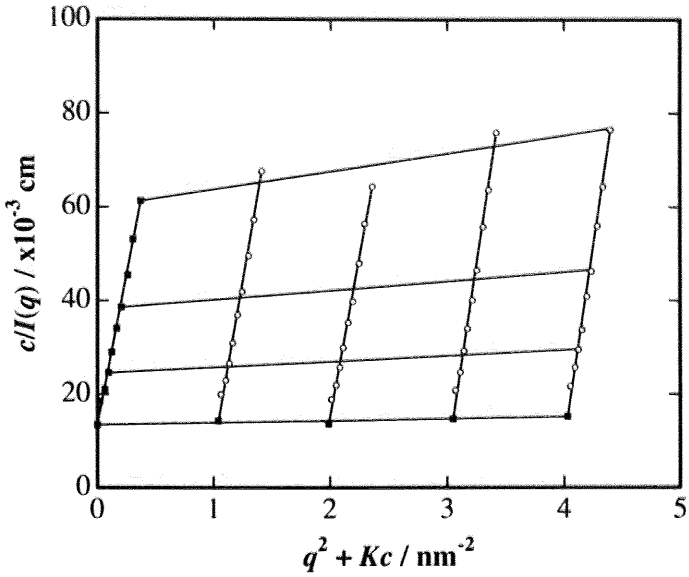

Figure 1.16: The Zimm plot of PS/cyclohexane solutions measured at 310 K. Here, $K = 1$ nm^{-2} g^{-1} ml is a constant.

out at 310 K, where the solution is the Θ condition.[22] The SANS data were analyzed with the Zimm equation given by

$$\frac{(b_1 v_0/v_1 - b_1)^2 N_A c}{I(q) m^2} = \frac{1}{M_w}\left[1 + \frac{1}{3}R_g^2 q^2 + ...\right] + 2A_2 c \tag{1.19}$$

where b_i and v_i are segment length and the molar volume of the polymer segment (i = P) and the solvent (i = S), m is the monomer molecular weight of the polymer, A_2 is the second virial coefficient, R_g is the radius of gyration, and c is the polymer concentration. Figure 1.16 shows the Zimm plot of the PS solutions. By extrapolating the data to $c = 0$ and $q = 0$, $M_w = 2.10 \times 10^4$ was obtained, which is in good agreement with the catalogue value by the supplier. The radius of gyration of the PS chains, R_g, were evaluated to be 3.89 nm, which is in accordance with the calculated value (4.02 nm) from the molecular weight with the following equation,[23,24]

$$R_g = 0.027 M_w^{1/2} [\text{nm}] \tag{1.20}$$

1.5 Conclusion

The SANS-U instrument was upgraded and the new performance was evaluated. (1) The new multi-wired area detector with a new data-acquisition system was installed,

enlarging the dynamic range of neutron counting with higher reliability. (2) The new control system, i.e., LabVIEW-based PC system, is a user-friendly interface with versatile possible-modifications compared with the old VAX-sequencer system. (3) An in-situ real-time circular averaging allows prompt evaluation of the experiment. The method of the absolute intensity calibration used at SANS-U was confirmed by calibration of the standard sample, Lupolen, with vanadium and water. (4) A focusing collimation system was installed. This system is advantageous for investigation of large samples than 10 mmϕ because of larger neutron flux without a loss of the q-resolution. (5) The performance of the upgraded SANS-U was examined by studying the molecular weight and the radius of gyration for a standard polystyrene sample. The new SANS-U will serve as a powerful SANS instrument for scientists from overseas as well as domestic users.

References

[1] Higgins, J. S.; Benoit, H. C. *Polymers and Neutron Scattering* Clarendon Press, Oxford, 1994.

[2] Schelten, J.; Wignall, G. D.; Ballard, D. G. H. *Polymer* 1974, **15**, 682–685.

[3] Glinka, C. J.; Barker, J. G.; Hammouda, B.; Krueger, S.; Moyer, J. J.; Orts, W. *J. Appl. Cryst.* 1998, **31**, 430–445.

[4] Ito, Y.; Imai, M.; Takahashi, S. *Physica B* 1995, **213 & 214**, 889–891.

[5] Heenan, R. K.; Penfold, J.; King, S. M. *J. Appl. Cryst.* 1997, **30**, 1140–1147.

[6] Otomo, T.; Furusaka, M.; Satoh, S.; Itoh, S.; Adachi, T.; Shimizu, S.; Takeda, M. *J. Phys. Chem. Sol.* 1999, **60**, 1579–1582.

[7] Friedrich, H., Wagner, V.; Wille, P. *Physica B* 1989, **156 & 157**, 547–549.

[8] Eskildsen, M. R.; Gammel, P. L.; Isaacs, E. D.; Detlefs, C.; Mortensen, K.; Bishop, D. J. *Nature* 1998, **391**, 563–566.

[9] Choi, S.-M.; Barker, J. G.; Glinka, C. J.; Cheng, Y. T.; Gammel, P. L. *J. Appl. Cryst.* 2000, **33**, 793–796.

[10] Noda, Y.; Utiki, T.; Kajitani, M. *J. Cryst. Soc. of Jpn.* 1983, **25**, 222–227.

[11] Takahashi, Y.; Noda, M.; Naruse, M.; Kanaya, T.; Watanabe, H.; Kato, T.; Imai, M.; Matsushita, Y. *J. Soc. Rheol. Jpn.* 2000, **28**, 187–191.

[12] Shibayama, M.; Isono, K.; Okabe, S.; Karino, T.; Nagao, M. *Macromolecules* 2004, **37**, 2909-2918.

[13] Nasimova, I. R.; Karino, T.; Okabe, S.; Nagao, M.; Shibayama, M. *J. Chem. Phys.* 2004, **121**, 9708–9715.

[14] Nasimova, I. R.; Karino, T.; Okabe, S.; Nagao, M.; Shibayama, M. *Macromolecules* 2004, **37**, 8721–8729.

[15] Matsuhita, Y. *private communication* 1995.

[16] Sears, V. F. *Neutron News* 1992, **3**, 29–37.

[17] Shibayama, M.; Nagao, M.; Okabe, S.; Karino, T. *J. Phy. Soc. Jpn.* 2005, **74**, 2728–2736.

[18] Wignall, G. D.; Bates, F. S. *J. Appl. Cryst.* 1987, **20**, 28–40.

[19] Mildner, D. F.; Carpenter, J. M. *J. Appl. Cryst.* 1984, **17**, 249–256.

[20] Hosemann, R.; Bagchi, S. N. *Direct Analysis of Diffraction by Matter*, North-Holland: Amsterdam, 1962.

[21] Shibayama, M.; Hashimoto, T. *Macromolecules* 1986, **19**, 740–749.

[22] Siporska, A.; Szydlowski, J.; Rebelo, L. P. N. *Phys. Chem. Chem. Phys.* 2003, **5**, 2996–3002.

[23] Cotton, J. P.; Decker, D.; Benoit, H.; Farnoux, B.; Higgins, J. S.; Jannink, G.; Ober, R.; Picot, C.; des Cloizeaux, J. *Macromolecules* 1974, **7**, 863.

[24] Melnichenko, Y. B.; Wignall, G. D.; Van Hook, A. W.; Szydlowski, J.; Wilczura, H.; Rebelo, L. P. *Macromolecules* 1998, **31**, 8436–8438.

Chapter 2

Evaluation of Incoherent Neutron Scattering from Softmatter

2.1 Introduction

SANS analyses on hydrogen-containing materials often encounter an uncertainty problem of incoherent scattering subtraction. This is because hydrogen has the largest incoherent scattering cross-section and the scattering signals having structure information may be buried by the scattering-angle-independent background, i.e., the incoherent scattering. In principle, the incoherent scattering can be estimated by calculation on the basis of the table of the cross-sections of the elements. However, the observed incoherent scattering intensity is dependent on the sample thickness. This is mainly due to multiple scattering. Schelten and Schmatz[1] discussed the effect of multiple scattering and proposed analytical expressions of multiple scattering from arbitrary scattering bodies. In the case of water, the so-called $(1 - T)$ correction has been widely employed for water samples up to 0.2 cm thick,[2,3] where T is the transmission of the sample. As its physical meaning is addressed by Wignall and Bates,[4] the scattering intensity from H_2O does not depend on its cross-sections but only on the transmission.

Various types of SANS analyses require well-qualified scattering intensity functions in the wide range of momentum transfer, q. Therefore, the incoherent scattering subtraction is very important in SANS data analyses. It is of particular importance when structure investigation is carried out with the contrast matching method using a mixture of protonated and deuterated solvents, e.g., a mixture of H_2O and D_2O, because of the large incoherent scattering from the protonated solvent (e.g., H_2O). May

et al.[3] discussed the incoherent scattering from mixtures of H_2O and D_2O as a function of composition, wavelength, and temperature, and found a linear relationship of the attenuation coefficient with the H-fraction. Dubner *et al.*[5] studied on deuterated and protonated mixtures of poly(ethylene terephthalate) (H-PET/D-PET) and reported that the incoherent scattering is proportional to the fraction of the H-PET. This result led to a proposal that the incoherent scattering intensity can be scaled with the factor $(1 - T)$. These findings, however, are restricted to a limited thickness (up to 0.2 cm) as well as low H-fractions (up to 0.6), and was not universal. Hence, in reality, incoherent scattering subtraction has been a "delicatessen" depending on individual scientists and/or institutions.[5–7] For example, in the case of polymer solutions in deuterated solvent, the incoherent scattering measured with bulk polymer or monomer is subtracted from the scattering intensity from the sample. However, each method has its own problem. In the case of the bulk polymer subtraction method, the incoherent scattering is very strong and a simple additivity rule does not work. The monomer subtraction method has uncertainty of the difference in mass densities between the monomer and the polymer, in addition to the volume change on mixing by dissolution. Estimation of incoherent scattering by calculation usually is much lower than the observed one. All of these problems are due to the fact that the "incoherent scattering" is dependent on the sample thickness even after normalization of sample thickness to the absolute intensity scale with a conventional method. Though the problem of multiple scattering in water has been extensively discussed in the past three decades,[2,5,8–10] it still remains as one of the unsolved problems.

In this chapter, a method to quantitatively estimate the sample thickness dependence of incoherent scattering is proposed. It will be shown that both transmission and incoherent scattering intensity are uniquely determined as a function of the cross-sections and the sample thickness by taking account of multiple scattering from hydrogen. The validity of the method is examined for mixtures of H_2O and D_2O, polyethylene having various sample thicknesses, and polymer solutions in D_2O. Examples of incoherent scattering intensity prediction are also provided.

2.2 Theoretical Background

2.2.1 Transmission

The incident neutron beam is attenuated during propagating in a scattering medium by scattering and absorption. The ratio of the transmitted neutron intensity, I_{tr} [s^{-1}], to the incident neutron intensity, I_0 [s^{-1}], is called the transmission, T ($= I_{tr}/I_0$). The transmission is experimentally obtained by measuring I_{tr} and I_0.

$$T \equiv \frac{I_{tr}}{I_0} = \exp(-\mu t), \tag{2.1}$$

where t [cm] is the sample thickness and μ [cm^{-1}] is the linear attenuation coefficient of the sample. μ is also evaluated by calculation with the following equation,

$$\mu = \sum_i \rho_i \sigma_{T,i}, \tag{2.2}$$

where ρ_i [cm^{-3}] and $\sigma_{T,i}$ [cm^2] are the number density and the total cross-section of the scattering element i. For compound i, ρ_i is given by

$$\rho_i = \frac{d_i N_A}{m_i}, \tag{2.3}$$

where d_i [$g \cdot cm^{-3}$] and m_i [$g \cdot mol^{-1}$] are the mass density and molecular weight of compound i, and N_A is the Avogadro's number. The total cross-section is the sum of the scattering cross-section, $\sigma_{s,i}$, and the absorption cross-section, $\sigma_{a,i}$. The scattering cross-section consists of the coherent scattering, $\sigma_{co,i}$, and the incoherent scattering cross-sections, $\sigma_{inc,i}$. Hence, $\sigma_{T,i}$ is given by

$$\sigma_{T,i} = \sigma_{s,i} + \sigma_{a,i} = \sigma_{co,i} + \sigma_{inc,i} + \sigma_{a,i}. \tag{2.4}$$

These values are easily calculated by consulting a table of cross-sections as listed in Table I.[11] For example, the total cross-sections of H_2O and D_2O are $\sigma_{T,H_2O} = 168.93 \times 10^{-24}$ cm^2 and $\sigma_{T,D_2O} = 19.52 \times 10^{-24}$ cm^2 for neutrons with the wavelength λ being 0.18 nm. Note that σ_a is proportional to λ and is given by

$$\sigma_a(\lambda) = \frac{\lambda}{0.18 \text{ nm}} \sigma_a(0.18 \text{ nm}), \tag{2.5}$$

where $\sigma_a(\lambda)$ and $\sigma_a(0.18$ nm) are the absorption cross-section at λ and at $\lambda = 0.18$ nm, respectively. It should be also noted that σ_{T,H_2O} is much larger than σ_{T,D_2O}. This is why the transmission of D_2O is much larger than H_2O, and multiple scattering has to be taken into account for scattering measurements from H–containing materials.

Table 2.1: Estimation of cross-sections for $\lambda = 0.70$ nm neutron. The units of the cross-section, σ, and the product of the number density and the cross-section, $\rho\sigma$, are barn ($=10^{-24}$ cm^2) and cm^{-1}, respectively.

	σ_{co}	σ_{inc}	σ_s	$\sigma_a(0.70\text{ nm})$	$\sigma_T(0.70\text{ nm})$	
H	1.7568	80.26	82.0168	1.293	83.33	
D	5.592	2.05	7.642	0.002	7.64	
C	5.551	0.001	5.552	0.014	5.57	
O	4.232	0.0008	4.2328	0.001	4.23	
N	11.01	0.5	11.51	7.389	19.00	
V	0.0184	5.08	5.0984	20.04	25.14	
	$\rho\sigma_{co}$	$\rho\sigma_{inc}$	$\rho\sigma_s$	$\rho\sigma_a(0.70\text{ nm})$	$\rho\sigma_T(0.70\text{ nm})$	$\rho\sigma_s/4\pi$
H_2O	0.259	5.369	5.628	0.087	5.714	0.448
D_2O	0.510	0.136	0.646	0.000	0.646	0.051
V	0.0013	0.348	0.350	1.374	1.724	0.028
PE	0.359	6.353	6.711	0.103	6.814	0.534
PNIPA	0.455	5.921	6.376	0.148	6.524	0.507

2.2.2 The incoherent scattering

The incoherent scattering from H–rich materials cannot be uniquely determined because of multiple scattering and inelastic scattering. Schelten and Schmatz[1] discussed the multiple scattering and derived an analytical expression for arbitrary scattering bodies. The theory was used to explain a distorted scattering function by multiple scattering. In the case that the coherent scattering cross-section is negligible and the incident neutron beam is mainly attenuated by incoherent scattering and by absorption, the following argument is widely accepted. The scattering intensity from a parallel-plate object with a thin enough thickness is given by Wignall and Bates,[4]

$$I(q) = \Phi_0 \varepsilon A \Delta\Omega \int_0^t \exp(-\rho\sigma_T x) \frac{\rho \mathrm{d}\sigma_s}{\mathrm{d}\Omega} \exp[-\rho\sigma_a(t-x)]\mathrm{d}x, \tag{2.6}$$

where Φ_0 [cm^{-2}s^{-1}], ε, A [cm^2], and $\Delta\Omega$ are the incident flux, the detector counting efficiency, the irradiated sample area, and the solid angle of the detector pixel, respectively. This equation means that the second (and subsequent) scattering is likely to give a roughly isotropic distribution of scattered neutron, and the effect of scattering of the once-scattered neutrons can be ignored.[12] This is why the total cross-section, σ_T, in the third part of the integrand of eq. 2.6 was replaced by the absorption cross-section, σ_a. A typical system to which this assumption may apply

is small-angle scattering from vanadium, where $\sigma_{co} \approx 0$ and $\sigma_{inc} \ll \sigma_a$ (See Table I). By conducting the integration, one obtains,

$$I(q) = \Phi_0 \varepsilon A \Delta\Omega \frac{\rho d\sigma_s}{d\Omega}[1 - \exp(-\rho\sigma_s t)] \frac{\exp(-\rho\sigma_a t)}{\rho\sigma_s}. \tag{2.7}$$

On the other hand, single scattering is simply given by,

$$I(q) = \Phi_0 \varepsilon A \Delta\Omega t \frac{\rho d\sigma_s}{d\Omega} \exp(-\rho\sigma_T t). \tag{2.8}$$

Hence, the ratio of the single-scattering to the total-scattering is given by

$$\frac{I(q)_{single}}{I(q)_{single} + I(q)_{multiple}} = \frac{\rho\sigma_s t \exp(-\rho\sigma_T t)}{\exp(-\rho\sigma_a t)[1 - \exp(-\rho\sigma_s t)]}. \tag{2.9}$$

This equation has been successfully employed for the incident beam calibration with vanadium.

In the case of H_2O, however, the scattering is predominantly incoherent, i.e., $\sigma_{inc} \gg \sigma_a \cong 0$. Wignall and Bates obtained the well-known empirical equation proposed by Jacrot[2,3] by substituting $\sigma_a \cong 0$ and $\exp(-\rho\sigma_s t) \approx T$ into eq. 2.7,

$$I(q) \cong \Phi_0 \varepsilon A \Delta\Omega \frac{\rho d\sigma_s}{d\Omega}(1 - T)\frac{1}{\rho\sigma_s} = \Phi_0 \varepsilon A \Delta\Omega \frac{(1 - T)}{4\pi}, \tag{2.10}$$

where $\rho d\sigma_s/d\Omega = \rho\sigma_s/4\pi$. Jacrot also considered the effect of inelastic scattering, i.e., the g-factor,[2]

$$g(\lambda) = \frac{1}{1 - \exp[-0.6\lambda^{1/2}]}. \tag{2.11}$$

Hence, the incoherent scattering from H-rich medium is given by

$$I(q) = \Phi_0 \varepsilon A \Delta\Omega \frac{(1 - T)}{4\pi} \frac{1}{1 - \exp[-0.6\lambda^{1/2}]}. \tag{2.12}$$

eq. 2.12 indicates that the scattering intensity is not proportional simply to $\rho d\sigma_s/d\Omega$ but to $(1 - T)$. eq. 2.12 has been frequently used to determine the incoherent scattering of H_2O with the thickness range from 0.05 to 0.2 cm.

Now let us rederive eq. 2.7 by properly taking acount of the multiple scattering. First, according to the treatment of Schelten and Schmatz,[1] one can re-write eq. 2.6 in the following form,

$$\begin{aligned} \frac{I_1(\mathbf{q})}{\varepsilon A \Delta\Omega} &\cong \Phi_0 \int_0^t \exp(-\mu x) \frac{\rho d\sigma_s}{d\Omega}(\mathbf{q}) \exp[-\mu(t - x)] dx \\ &= \Phi_0 \exp(-\mu t) t \frac{\rho d\sigma_s}{d\Omega}(\mathbf{q}), \end{aligned} \tag{2.13}$$

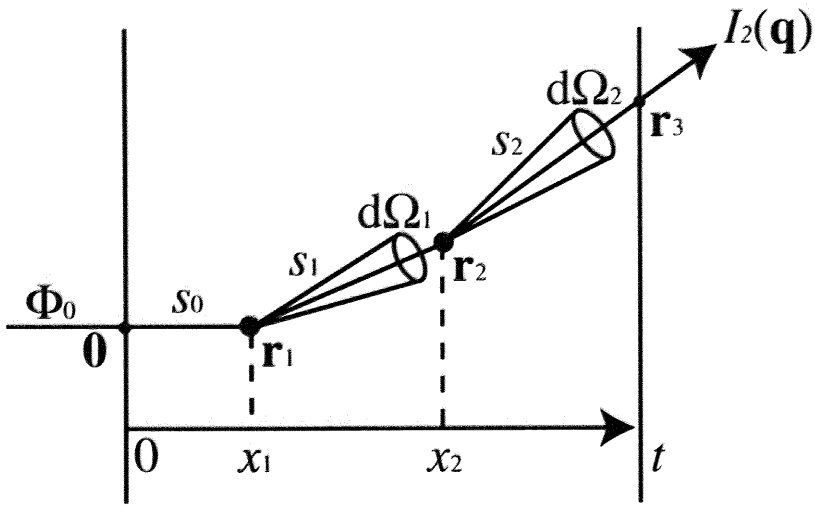

Figure 2.1: Twice-scattering in a specimen with thickness t. The incident neutron enters the specimen at $\mathbf{0}$ and scatters at $\mathbf{r}_1$ and $\mathbf{r}_2$, and then exits at $\mathbf{r}_3$. s_0, s_1, and s_2 are the distances given by $s_0 = |\mathbf{r}_1 - \mathbf{0}|$, $s_1 = |\mathbf{r}_2 - \mathbf{r}_1|$, and $s_2 = |\mathbf{r}_3 - \mathbf{r}_2|$, respectively. The projections of $\mathbf{r}_1$ and $\mathbf{r}_2$ on the thickness direction are x_1 and x_2.

where $I_1(\mathbf{q})$ means the single-scattering at the scattering vector $\mathbf{q}$. Note that $(\mathrm{d}\sigma_\mathrm{s}/\mathrm{d}\Omega)(\mathbf{q})$ is $\mathbf{q}$-dependent. When a twice-scattering takes place, attenuation of the neutron flux in the specimen is scattering-path dependent. Suppose a twice-scattering takes place at $\mathbf{r} = \mathbf{r}_1$ and at $\mathbf{r} = \mathbf{r}_2$ as shown in Fig. 2.1, the scattering intensity is given by

$$\begin{aligned}\frac{I_2(\mathbf{q})}{\varepsilon A \Delta\Omega} &= \Phi_0 \int_{4\pi}\int_{s_0}\int_{s_1}\int_{s_2} \exp(-\mu s_0)\mathrm{d}s_0 \frac{\rho \mathrm{d}\sigma_\mathrm{s}}{\mathrm{d}\Omega}(\mathbf{q}_1)\mathrm{d}\Omega_1 \\ &\times \exp(-\mu s_1)\mathrm{d}s_1 \frac{\rho \mathrm{d}\sigma_\mathrm{s}}{\mathrm{d}\Omega}(\mathbf{q}-\mathbf{q}_1) \\ &\times \exp(-\mu s_2)\mathrm{d}s_2. \end{aligned} \tag{2.14}$$

Here, Ω_1 is the solid angle of the scattered neutron at $\mathbf{r} = \mathbf{r}_1$ and $\mathrm{d}\Omega_1 = \mathrm{d}\mathbf{q}_1/(2\pi/\lambda)^2$. s_0, s_1, and s_2 are the distances of a propagating neutron between the corresponding points as shown in Fig. 2.1. Note that the path integrations in eq. 2.14 have to be carried out with respect to the all possible paths but only in the specimen with the restriction of the final scattering vector being $\mathbf{q}$. When the incoherent scattering cross-section is large, contribution of a multiple scattering becomes large. However, a multiple-scattering intensity including a large-angle scattering decays much faster than the case without a large-angle scattering. Hence, the scattering-path integrations can be assumed to the thickness integrations with respect to x_1 and x_2. Accordingly, eq. 2.14 is simply expressed in a form with one-dimensional integration as

was proposed by Schelten and Schmatz[1] ,

$$\begin{aligned}\frac{I_2(\mathbf{q})}{\varepsilon A\Delta\Omega} &\cong \Phi_0 \int_{4\pi}\int_0^t\int_{x_1}^t \exp(-\mu x_1)\mathrm{d}x_1 \frac{\rho \mathrm{d}\sigma_\mathrm{s}}{\mathrm{d}\Omega}(\mathbf{q}_1)\mathrm{d}\Omega_1 \\ &\times \exp[-\mu(x_2-x_1)]\mathrm{d}x_2 \frac{\rho \mathrm{d}\sigma_\mathrm{s}}{\mathrm{d}\Omega}(\mathbf{q}-\mathbf{q}_1) \\ &\times \exp[-\mu(t-x_2)]. \end{aligned} \tag{2.15}$$

Note that eq. 2.15 is decoupled to two integrations, one with respect to the scattering and the other to attenuation. The former takes account of scattering to any direction, while the latter assumes attenuation by absorption and scattering along the sample-thickness direction.

For incoherent scattering and/or coherent scattering from a homogeneous medium consisting of small molecules, such as H_2O, the small-angle scattering is **q**-independent. Hence, eq. 2.13 reads

$$\frac{I_1(q)}{\varepsilon A\Delta\Omega} = \Phi_0 \exp(-\mu t) t \frac{\rho\sigma_\mathrm{s}}{4\pi}. \tag{2.16}$$

Similarly, the **q**-integration for the twice scattering in eq. 2.15 is written by,

$$\begin{aligned}\int_{4\pi} \frac{\rho \mathrm{d}\sigma_\mathrm{s}}{\mathrm{d}\Omega}(\mathbf{q}_1)\frac{\rho \mathrm{d}\sigma_\mathrm{s}}{\mathrm{d}\Omega}(\mathbf{q}-\mathbf{q}_1)\mathrm{d}\Omega_1 &= \left(\frac{\rho\sigma_\mathrm{s}}{4\pi}\right)^2 \int_{4\pi}\mathrm{d}\Omega \\ &= 4\pi\left(\frac{\rho\sigma_\mathrm{s}}{4\pi}\right)^2. \end{aligned} \tag{2.17}$$

On the other hand, the integration over the thicknesses gives,

$$\begin{aligned}&\int_0^t\int_{x_1}^t \exp(-\mu x_1)\mathrm{d}x_1 \exp[-\mu(x_2-x_1)]\mathrm{d}x_2 \exp[-\mu(t-x_2)] \\ &\qquad = \exp(-\mu t)\int_0^t (t-x_1)\mathrm{d}x_1 = \exp(-\mu t)\frac{t^2}{2}. \end{aligned} \tag{2.18}$$

Hence,

$$\frac{I_2(q)}{\varepsilon A\Delta\Omega} = \Phi_0 \exp(-\mu t)\frac{1}{2}t^2\frac{1}{4\pi}\left(\rho\sigma_\mathrm{s}\right)^2. \tag{2.19}$$

Similarly, for the n–times scattering, one obtains

$$\frac{I_\mathrm{n}(q)}{\varepsilon A\Delta\Omega} = \Phi_0 \exp(-\mu t)\frac{1}{n!}t^n\frac{1}{4\pi}\left(\rho\sigma_\mathrm{s}\right)^n. \tag{2.20}$$

By summing up the n–times scattering, one obtains

$$\frac{I(q)}{\varepsilon A\Delta\Omega} = \Phi_0 \exp(-\mu t)\frac{1}{4\pi}\sum_{n=1}^{\infty}\frac{1}{n!}\left(\rho\sigma_\mathrm{s}t\right)^n. \tag{2.21}$$

The summation is carried out to

$$\sum_{n=1}^{\infty}\frac{1}{n!}x^n = x + \frac{1}{2!}x^2 + \cdots = \sum_{n=0}^{\infty}\frac{1}{n!}x^n - 1 = e^x - 1. \tag{2.22}$$

Therefore, the scattering intensity with multiple scattering correction is given by

$$\frac{I(q)}{\varepsilon A \Delta\Omega} = \Phi_0 \exp(-\mu t) \frac{\rho\sigma_s t}{4\pi} \frac{\exp(\rho\sigma_s t) - 1}{\rho\sigma_s t}. \tag{2.23}$$

Note that eq. 2.23 is identical to eq. 2.7 because $\mu \equiv \sigma_T$. Here, let us briefly discuss the reason why the two equations are identical. In the derivation of eq. 2.7, the following conjecture was made. Neutrons removed from a particular detector element by multiple scattering are replaced by an equal number of neutrons multiply scattered into this detector element from other angles. Therefore, attenuation of the scattered beam due to multiple scattering processes is ignored and only absorption loss is allowed for on the scattered beam.[4] These statements are easily understood by substituting $\sigma_a = 0$ in eq. 2.9. The relation between single and total scattering corresponds to the transmitted and scattered neutrons with factors of T and $(1 - T)$, respectively. On the other hand, eq. 2.23 is derived by properly considering multiple scattering, and has a clear physical implication. Let us examine eq. 2.23 more carefully. It is a product of the neutron flux, the transmission, the differential scattering cross-section, and the correction factor, C necessary for multiple scattering given by

$$C \equiv \frac{I(q)}{I_1(q)} = \frac{\exp(\rho\sigma_s t) - 1}{\rho\sigma_s t} \equiv \frac{e^{Kt} - 1}{Kt}. \tag{2.24}$$

where K [cm^{-1}] is denoted to be $K \equiv \rho\sigma_s$. Note that the correction factor is sample-thickness dependent.

It is quite important to compare the two factors, i.e., the Jacrot's factor $(1 - T)$ and the multiple-scattering factor (this work). eqs. 2.9 and 2.23 can be rewritten as

$$\frac{4\pi I(q)}{\Phi_0 \varepsilon A \Delta\Omega} \frac{1}{TKt} = \frac{1 - T}{TKt} \text{ (Jacrot)}, \tag{2.25}$$

$$\frac{4\pi I(q)}{\Phi_0 \varepsilon A \Delta\Omega} \frac{1}{TKt} = \frac{e^{Kt} - 1}{Kt} \text{ (This work)}. \tag{2.26}$$

Fig. 2.2 shows the comparison of the two factors for the cases of (a) H_2O and (b) vanadium. The former demonstrates the case of $\sigma_s \gg \sigma_a (\approx 0)$, and the latter does $\sigma_a \gg \sigma_s (\approx \sigma_{inc} > 0)$. The values of the cross-sections for comparison were taken from Table I. As shown in the figure, the $(1 - T)$ factor is applicable only at the limit of $t \to 0$ and a significant deviation from the multiple-scattering factor occurs even at $t = 0.1$cm. On the other hand, the $(1 - T)$ factor is not applicable to an estimation of incoherent scattering for materials with a large absorption cross-sections such as

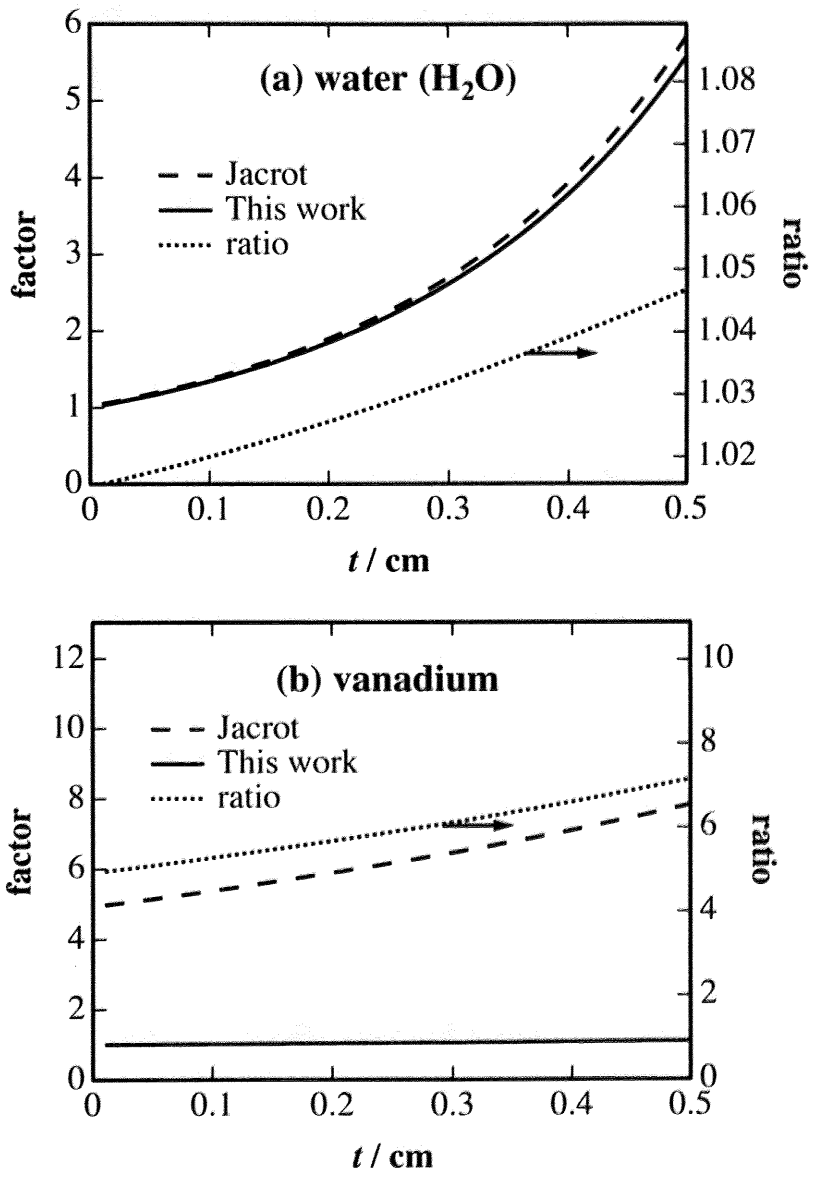

Figure 2.2: Comparison of the factors, $(1-T)/TKt$ (eq. 2.25) and $(e^{Kt}-1)/Kt$ (eq. 2.26), for (a) multiple-scattering dominant and (b) absorption dominant materials.

vanadium. The factor derived in this work is applicable to both multiple scattering-dominant and absorption-dominant cases because the two factors are properly taken into account.

2.3 Experimental

2.3.1 Samples

As hydrogen-rich scatters, polyethylene (PE) and water samples were prepared. Low density polyethylene (FW–200–0) was kindly provided by Sumitomo Chemical Co. Thin slabs of 0.1 (0.106), 0.2 (0.188), and 0.3 (0.291) cm thick were prepared by melt–pressing. Here, the numbers outside and inside of the parentheses denote the nominal and exact thicknesses, respectively. The mass density of the PE sample was $d = 0.922$ g/cm^3. A 0.4 cm-thick PE sample was prepared by stacking 2 of 0.2 cm-thick PE sheets. As for water samples, mixtures of H_2O and D_2O were filled in quartz cells. The water compositions were varied from 0 to 100 vol.% H_2O. The cell thicknesses were also varied from 0.1 to 0.2, 0.3, and 0.4 cm. The deuterated water with 99.9 at.%D was purchased from Isotec Inc, U.S.A.

2.3.2 SANS

SANS experiments were carried out at the SANS-U. The incident neutron wavelength λ was 0.70 nm with the wavelength distribution of 10 % (FWHM), and the sample to detector distance was 1 m for the water mixtures and 2 m for PE. The source aperture was 20 mm$^{\phi}$ and was placed by 4 m apart from the sample and the sample slit was 5 mm$^{\phi}$. The covered momentum transfer, q, was ranged from 0.02 to 0.3 Å^{-1}. The transmission of neutron beam was counted with a ^{3}He detector placed at the center of the transmitted beam just before the PSD. The transmissions of the samples with various thicknesses were obtained by measuring the transmitted neutrons with and without the samples for 30 s. The measurements were carried out three times each and arithmetic averages were taken. The scattered neutrons detected on the area detector were circularly averaged and the scattering intensity function, $I(q)$, was obtained as a function of q. The sample scattering, I_{SAM} [s^{-1}], was corrected for the blocked beam scattering I_{BGD} (BGD; B_4C), the sample thickness, t_{SAM} [cm], open beam scattering, I_{OPEN} (OPEN), and transmission, T_{SAM}, with the

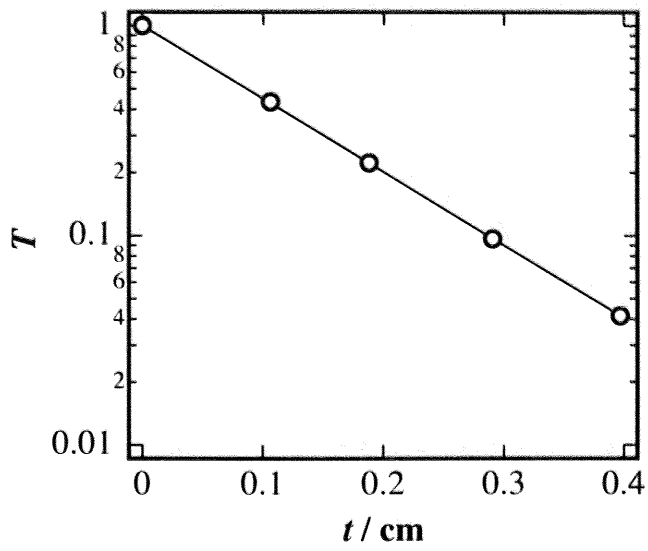

Figure 2.3: Semi-logarithmic plot of the transmission, T, of polyethylene (PE) samples having different thicknesses.

following equation, and then scaled to the absolute intensity,

$$\left(\frac{d\Sigma}{d\Omega}\right)_{SAM} = \frac{\frac{I_{SAM}-I_{BGD}}{T_{SAM}} - (I_{OPEN}-I_{BGD})}{t_{SAM}\times\cos^3 2\theta} \times \frac{0.0573}{I^0_{STD}}, \qquad (2.27)$$

$$I^0_{STD} = \frac{(I_{STD}-I_{BGD}) - (I_{OPEN}-I_{BGD})\times T_{STD}}{\cos^3 2\theta},$$

where I_{STD} [s^{-1}] and T_{STD} are the scattering intensity and the transmission of the standard sample. $\cos^3 2\theta$ is the correction factor for oblique incidence and 2θ is the scattering angle. In this experiment, the polyethylene standard sample (Lupolen) was used and the numerical constant in eq. 2.27 was obtained by calibrating with the vanadium scattering.[13]

2.4 Results and Discussion

2.4.1 Polyethylene (PE)

First of all, let us examine the validity of eq. 2.23 from the viewpoint of sample thickness dependence by using PE samples having different sample thicknesses. The transmission of PE is plotted as a function of the sample thickness, t, in Fig. 2.3. As shown in the plot, the data fall on to a single straight line in the semi-logarithmic plot. Note that Lambert-Beer law holds a wide absorption range down to the transmission

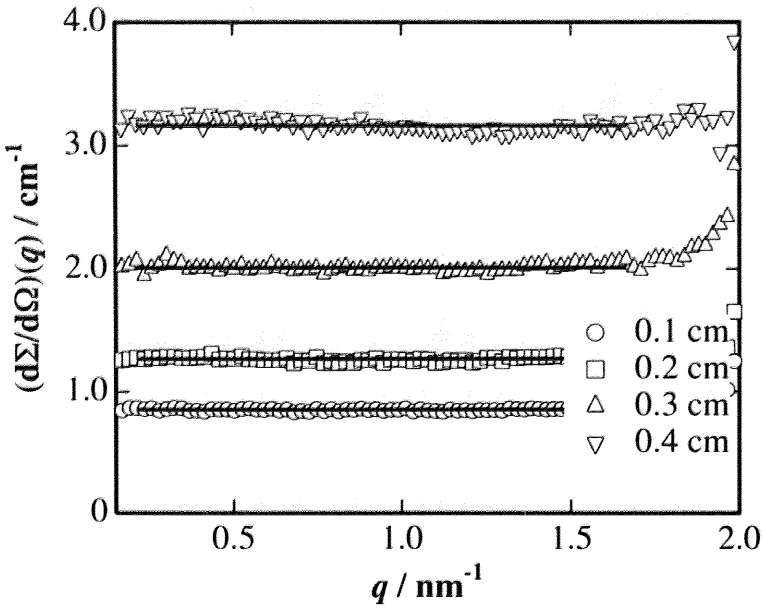

Figure 2.4: The observed scattering intensity, $(d\Sigma/d\Omega)(q)$, of PE with different thicknesses.

of ca. 5 %. From the linear curve fitting, the following equation is obtained,

$$T = \exp(-\mu_{\rm PE} t), \tag{2.28}$$

with $\mu_{\rm PE,obs} = 8.02$ cm^{-1}. The calculated value with eq. 2.2 is $\mu_{\rm PE,cal} = 6.814$ cm^{-1}. Hence, the observed one is about 18 % larger than the calculated one. Though this may be mainly due to multiple scattering, no plausible explanation has not been obtained.

Fig. 2.4 shows the absolute scattering intensity, $(d\Sigma/d\Omega)(q)$, for PEs having various sample thicknesses. $(d\Sigma/d\Omega)(q)$ is independent of q as is the case of incoherent scattering. However, the observed $(d\Sigma/d\Omega)(q)$ is an increasing function of t even that $(d\Sigma/d\Omega)(q)$ is corrected for the sample thickness and transmission. (See eq. 2.27.) Hence, the observed $(d\Sigma/d\Omega)(q)$ cannot be a material (intensive) property. Certainly, this contradiction is ascribed to the multiple scattering.

In order to clarify the general rule of the incoherent scattering from hydrogen–rich objects, the mean value of $(d\Sigma/d\Omega)(q)$s, i.e., $\langle (d\Sigma/d\Omega)(q) \rangle \equiv \sum_{\rm i}^{n} (d\Sigma/d\Omega)(q_{\rm i})/N$, was plotted as a function of the sample thickness, where $N(\approx 80)$ is the number of data points used for evaluation of the incoherent scattering. Fig. 2.5 shows the

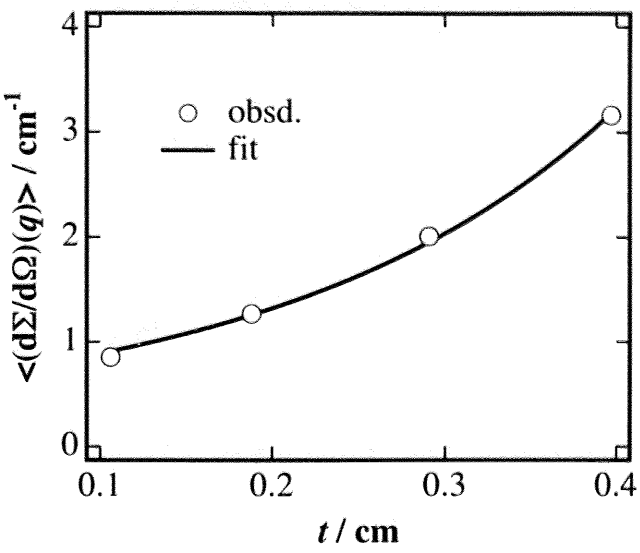

Figure 2.5: Variation of $\langle(\mathrm{d}\Sigma/\mathrm{d}\Omega)(q)\rangle$ with sample thickness for PEs. The solid line denotes the fitting function with eq. 2.23.

sample–thickness dependence of $\langle(\mathrm{d}\Sigma/\mathrm{d}\Omega)(q)\rangle$ with the fit with eq. 2.23, i.e,

$$\begin{aligned}
\left\langle \frac{\mathrm{d}\Sigma}{\mathrm{d}\Omega}(q) \right\rangle &= \frac{I(q)}{\varepsilon A \Delta\Omega \Phi_0 t \exp(-\mu t)} = \left\langle \frac{\mathrm{d}\Sigma}{\mathrm{d}\Omega}(q) \right\rangle_0 C, \\
\left\langle \frac{\mathrm{d}\Sigma}{\mathrm{d}\Omega}(q) \right\rangle_0 &= \frac{K}{4\pi} = \frac{\rho\sigma_\mathrm{s}}{4\pi}, \\
C &= \frac{e^{Kt} - 1}{Kt},
\end{aligned} \tag{2.29}$$

where $\langle(\mathrm{d}\Sigma/\mathrm{d}\Omega)(q)\rangle_0$ is the differential scattering cross-section at single-scattering limit, and C is the correction factor. Those values obtained by the fit are $\langle(\mathrm{d}\Sigma/\mathrm{d}\Omega)(q)\rangle_{0,\mathrm{obs}} = 0.622$ cm^{-1} and $K_{\mathrm{PE,obs}} = 6.76$ cm^{-1}, while the calculated values for PE are 0.534 cm^{-1} and $K_{\mathrm{PE,calc}} = 6.71$ cm^{-1}, respectively. Hence, the agreement for K between the calculated and observed values is quite satisfactory. On the other hand, the observed value of $\langle(\mathrm{d}\Sigma/\mathrm{d}\Omega)(q)\rangle_0$ is 16 % larger than the calculated one. This may be mainly due to the error of the accuracy of the absolute intensity calibration since this is a calibration-dependent and instrument-dependent variable.

Fig. 2.6 shows the corrected $(\mathrm{d}\Sigma/\mathrm{d}\Omega)(q)$s for PEs with eq. 2.23. As shown in the figure, all of the $(\mathrm{d}\Sigma/\mathrm{d}\Omega)(q)$s are nicely collapsed to each other. This strongly suggests that the sample–thickness dependence of the incoherent scattering can be corrected with the correction factor given by eq. 2.24.

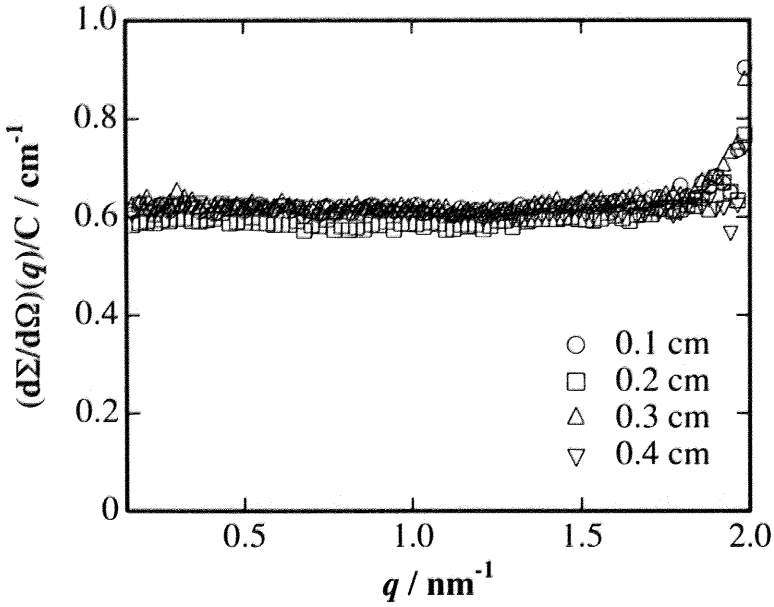

Figure 2.6: Corrected $(\mathrm{d}\Sigma/\mathrm{d}\Omega)(q)$s of PE with the new correction factor, $(e^{Kt}-1)/Kt$.

2.4.2 Water mixtures

A similar analysis to the incoherent scattering of PE *was carried out for mixtures of* light and heavy water. This example allows to examine the validity of eq. 2.23 for the case where the contribution of incoherent and coherent scattering varies as a function of composition. In Fig. 2.7 the obtained transmission is plotted as a function of the volume fraction of water f_{H}. As shown in the figure, the data points fall on a straight line for each composition from $f_{\mathrm{H}} = 0$ to 1. Introducing Lambert-Beer's relation, the transmission can be written by the following equation,

$$T = \frac{I_{\mathrm{tr}}}{I_0} = \exp[-t\{\mu_{\mathrm{H}} f_{\mathrm{H}} + \mu_{\mathrm{D}}(1 - f_{\mathrm{H}})\}], \tag{2.30}$$

where μ_{H} and μ_{D} are the absorption coefficients of H_2O and D_2O, respectively. Taking logarithm and dividing with t for both sides of eq. 2.30, linear functions of f_{H} were obtained for the normalized attenuation coefficient, $F(f_{\mathrm{H}})$, for the water mixtures with the four different thicknesses,

$$F(f_{\mathrm{H}}) \equiv \frac{\ln T}{-t} = (\mu_{\mathrm{H}} - \mu_{\mathrm{D}}) f_{\mathrm{H}} + \mu_{\mathrm{D}}. \tag{2.31}$$

Fig. 2.8 shows the variations of $F(f_{\mathrm{H}})$ for the four different sample thicknesses. Again, all of the lines are collapsed to a single straight line, from which the values of

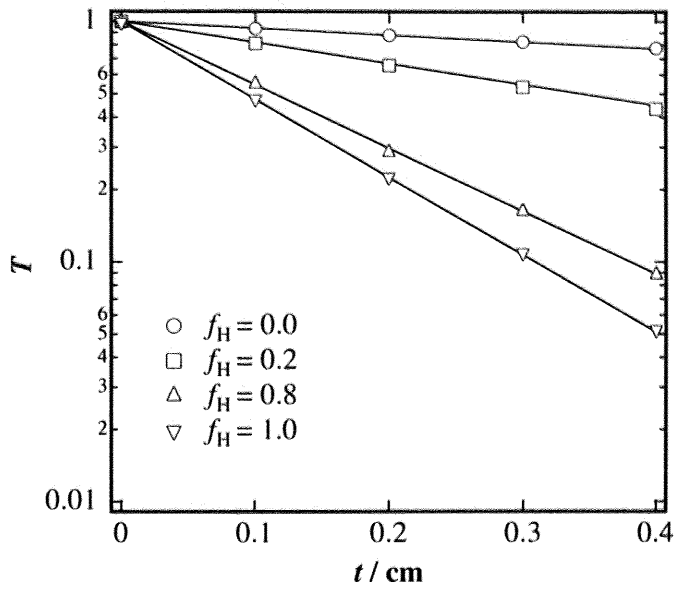

Figure 2.7: Semi-logarithmic plot of the transmission, T, of H_2O and D_2O mixtures having various sample thicknesses. The sample thicknesses are 0.1, 0.2, 0.3, and 0.4 cm. f_H is the volume fraction of H_2O.

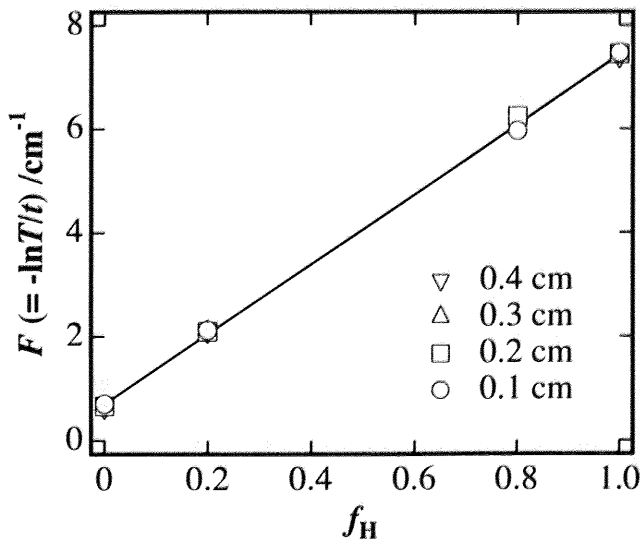

Figure 2.8: The normalized log-transmission, $\ln T$, with respect to the sample thickness, t. All of the four lines are collapsed to one straight line.

μ_H (H_2O) and μ_D (D_2O) were obtained to be $\mu_H = 6.22$ cm^{-1} and $\mu_D = 0.588$ cm^{-1}. These values are in good agreement with the calculated values for H_2O and D_2O, i.e., $\mu_{H,calc} = 5.714$ cm^{-1} and $\mu_{D,calc} = 0.646$ cm^{-1}. Dubner *et al.*[5] obtained a similar relationship with eq. 2.30, but the sample thickness was restricted to 0.2 cm. eq. 2.31 indicates that the transmission of any kind of hydrogen containing objects can be predicted by knowing the hydrogen number density in the sample. This finding is particularly important for SANS experiments using a contrast-matching method since the hydrogen concentrations are significantly large.

Fig. 2.9 shows $(d\Sigma/d\Omega)(q)$s of H_2O and D_2O mixtures with various compositions. The sample thicknesses were (a) 0.1 cm and (b) 0.4 cm. Note that the average value of the observed incoherent scattering intensity from 0.1 cm thick H_2O was $\langle(d\Sigma/d\Omega)(q)\rangle = 0.892$ cm^{-1}. The reported values of $\langle(d\Sigma/d\Omega)(q)\rangle$ with $\lambda = 0.70$ nm for H_2O are 0.89 and 1.01 cm^{-1}, respectively at the Institute of Laue-Langevin (ILL) and at the National Institute of Standards and Technology (NIST).[14] Although, the obtained value, i.e., $\langle(d\Sigma/d\Omega)(q)\rangle = 0.892$ cm^{-1} is somewhat smaller than those values in the literature, the agreement is satisfactory. Now, let us discuss the thickness dependence of $\langle(d\Sigma/d\Omega)(q)\rangle$ for the water mixtures.

Fig. 2.10 shows the thickness dependence of $\langle(d\Sigma/d\Omega)(q)\rangle$ for the water mixtures with $f_H = 0$, 0.2, 0.8 and 1.0. Again, all of the lines can be described by eq. 2.23. The typical fitted values of $\langle(d\Sigma/d\Omega)(q)\rangle_0$ and K are $\langle(d\Sigma/d\Omega)(q)\rangle_{0,H_2O} = 0.689$ cm^{-1} and $K_{H_2O} = 5.40$ cm^{-1} and $\langle(d\Sigma/d\Omega)(q)\rangle_{0,D_2O} = 0.0302$ cm^{-1} and $K_{D_2O} = 0.578$ cm^{-1}. The values for the other compositions are given in Table II. Hence, it can be concluded that $(d\Sigma/d\Omega)(q)$s for water mixtures are also simply given by eq. 2.23. The observed values are somewhat larger and smaller than the calculated values, respectively. The agreement between the observed and calculate values for PE is much better than for H_2O. Therefore, the discrepancy found in H_2O is deduced to be mainly originating from the inelastic scattering of H_2O.

Apart from the discussion of the absolute values of the $\langle(d\Sigma/d\Omega)(q)\rangle_{0,H_2O}$, the above discussion indicates that the incoherent scattering from a mixture of H_2O and D_2O can be written by

$$\left\langle \frac{d\Sigma}{d\Omega}_{water}(q) \right\rangle = \left\langle \frac{d\Sigma}{d\Omega}_{water}(q, f_H) \right\rangle_0 \frac{\exp[K(f_H)t] - 1}{K(f_H)t}. \tag{2.32}$$

Here, $K = K(f_H)$ is now a function of f_H. Fig. 2.11 shows the reduced incoherent

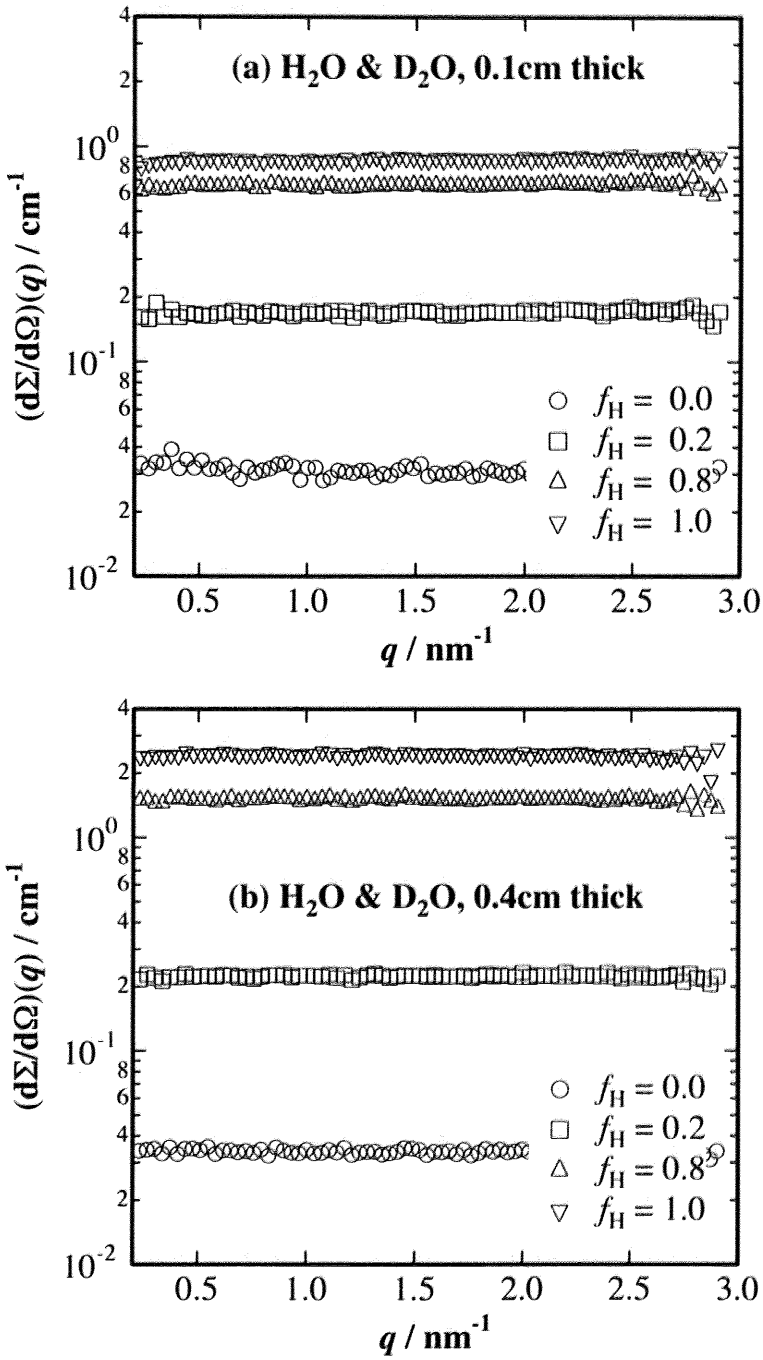

Figure 2.9: The observed scattering intensity, $(d\Sigma/d\Omega)(q)$, of H_2O and D_2O mixtures with the sample thickness of (a) 0.1 cm and (b) 0.4 cm. f_H is the volume fraction of H_2O.

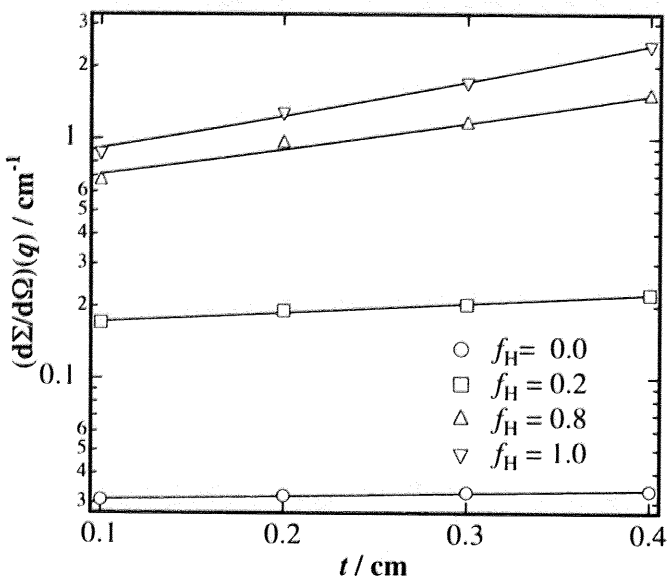

Figure 2.10: Thickness dependence of $\langle(\mathrm{d}\Sigma/\mathrm{d}\Omega)(q)\rangle$ of H_2O and D_2O mixtures with various f_Hs.

Table 2.2: Comparison of the observed differential cross-sections at single-scattering limit with the calculated values for light- and heavy-water mixtures. The numbers in the parenthesis are the calculated values with eq. 2.35.

f_H	$\left\langle \frac{\mathrm{d}\Sigma}{\mathrm{d}\Omega}(q) \right\rangle_0$ [cm^{-1}]	K[cm^{-1}]
0	0.0302 (0.051)	0.578 (0.646)
0.2	0.159 (0.131)	1.63 (1.642)
0.8	0.568 (0.369)	4.29 (4.632)
1	0.689 (0.448)	5.40 (5.628)

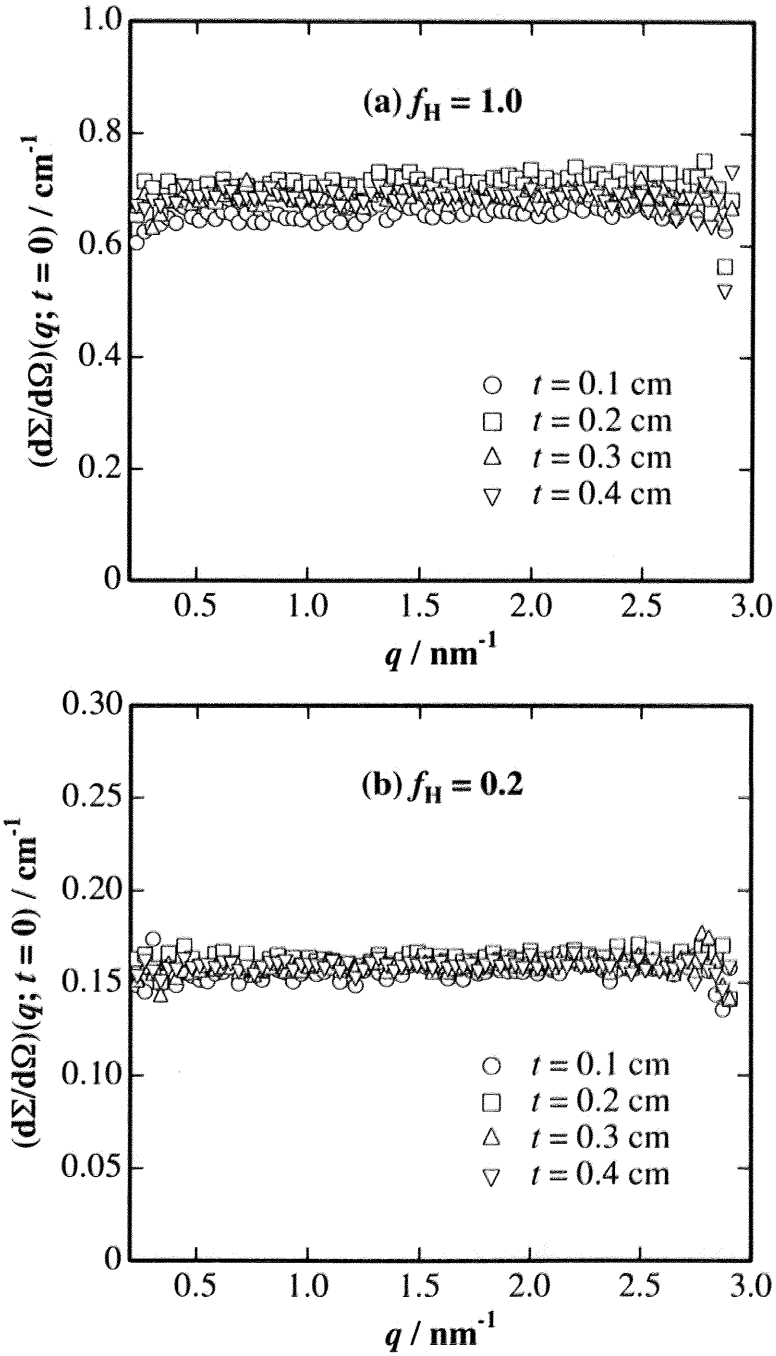

Figure 2.11: Reduced scattering intensities of (a) H_2O ($f_H = 1.0$) and (b) a mixture of H_2O and D_2O ($f_H = 0.2$) with various sample thicknesses. The correction factors, $(e^{Kt} - 1)/Kt$, are (a) $K = 5.40$ cm^{-1} and (b) $K = 1.63$ cm^{-1}.

scattering intensity for (a) H_2O ($f_H = 1.0$) and (b) a mixture with $f_H = 0.2$ with different thicknesses. All curves are nicely overlapped to each other for both $f_H = 0.2$ and 1.0. By substituting the observed values, the incoherent scattering of light water with a given thickness is now predicted by,

$$\left\langle \frac{d\Sigma}{d\Omega_{H_2O}}(q) \right\rangle = 0.689 \frac{\exp[5.40t] - 1}{5.40t} [\mathrm{cm}^{-1}]. \tag{2.33}$$

This equation covers the incoherent scattering from water with $t \leq 0.4$ cm. By using eq. 2.33, one obtains $\langle (d\Sigma/d\Omega)(q) \rangle = 0.911$ cm^{-1} with $t = 0.1$ cm and 1.232 cm^{-1} with $t = 0.2$ cm for $\lambda = 0.70$ nm neutrons. Wignall and Bates reported $\langle (d\Sigma/d\Omega)(q) \rangle = 0.937$ cm^{-1} with $t = 0.1$ cm and 1.303 cm^{-1} with $t = 0.2$ cm for $\lambda = 0.475$ nm neutrons at Oak Ridge National Laboratory (ORNL).[4] Hence, the agreement is satisfactory. Now, having the success of this argument, let us generalize the discussion and propose equations describing the incoherent scattering from hydrogen–containing media.

2.4.3 Generalization H-containing materials

On the basis of the experimental findings and discussion, let us generalize eq. 2.32 to H-containing materials. Now, the incoherent scattering can be approximated by the incoherent scattering from the hydrogen in the system, namely

$$\frac{d\Sigma}{d\Omega} \approx \left\langle \frac{d\Sigma}{d\Omega_H} \right\rangle_0 \frac{\exp[K_H t] - 1}{K_H t}. \tag{2.34}$$

Here, $\langle (d\Sigma/d\Omega)_H \rangle_0$ is the differential incoherent scattering cross-section at single-scattering limit of hydrogen in the system. The values of $\langle (d\Sigma/d\Omega)_{inc,H} \rangle_0$ and K_H can be easily obtained by summing up the values of cross–sections of the hydrogen in the components as shown in Table II,

$$K_H \approx \sum_i \rho_i (\sigma_H)_i, \quad \left\langle \frac{d\Sigma}{d\Omega_H} \right\rangle_0 = \frac{K_H}{4\pi}. \tag{2.35}$$

Thus, the incoherent scattering for an arbitrary system containing hydrogen is predicted.

2.4.4 Diluted systems

Let us further generalize the equation to dilute systems, e.g., a polymer solution in deuterated solvent, where the hydrogen number density is considerably low compared

with the cases discussed above and the product of the number density and the cross–section of the hydrogen is comparable to those of the other components. Hence,

$$\left\langle \frac{\mathrm{d}\Sigma}{\mathrm{d}\Omega_{\mathrm{solution}}}(q) \right\rangle = \left\langle \frac{\mathrm{d}\Sigma}{\mathrm{d}\Omega_{\mathrm{solution}}}(q) \right\rangle_0 \frac{\exp[K_{\mathrm{solution}}t] - 1}{K_{\mathrm{solution}}t}, \tag{2.36}$$

and

$$K_{\mathrm{solution}} = \sum_{\mathrm{i}} \rho_{\mathrm{i}} \left(\sigma_{\mathrm{s}}\right)_{\mathrm{i}} = \rho_{\mathrm{solute}}\sigma_{\mathrm{s,solute}} + \rho_{\mathrm{solvent}}\sigma_{\mathrm{s,solvent}}, \tag{2.37}$$

$$\left\langle \frac{\mathrm{d}\Sigma}{\mathrm{d}\Omega_{\mathrm{solution}}}(q) \right\rangle_0 = \frac{K_{\mathrm{solution}}}{4\pi}. \tag{2.38}$$

Let us give an example, a 7.8 vol% poly(N-isopropylacrylamide) (PNIPA) -(-$C_6H_{11}ON$-)$_n$- solution in deuterated water. PNIPA has $m_{\mathrm{PNIPA}} = 113.16$ g/mol, $d_{\mathrm{PNIPA}} = 1.26$ g/cm^3 and the number of hydrogen per monomer is 11. Hence, the following values are obtained,

$$\begin{aligned} K_{\mathrm{NIPAsoln}} &= 6.376 \times 0.078 + 0.646 \times 0.922 \\ &= 1.093[\mathrm{cm}^{-1}], \end{aligned} \tag{2.39}$$

and

$$\left\langle \frac{\mathrm{d}\Sigma}{\mathrm{d}\Omega_{\mathrm{NIPAsoln}}} \right\rangle_0 = 0.0870[\mathrm{cm}^{-1}]. \tag{2.40}$$

As a result, the incoherent scattering for 7.8 vol% PNIPA solution in D_2O with 0.4 cm thick is given by

$$\frac{\mathrm{d}\Sigma}{\mathrm{d}\Omega_{\mathrm{NIPAsoln}}} \approx \left\langle \frac{\mathrm{d}\Sigma}{\mathrm{d}\Omega_{\mathrm{NIPAsoln}}} \right\rangle_0 \frac{\exp(1.093t) - 1}{1.093t} = 0.109[\mathrm{cm}^{-1}]. \tag{2.41}$$

The observed values are 0.09 - 0.13 cm^{-1}.[15] The agreement is quite satisfactory.

At the end of the discussion, it should be noted that the $(1 - T)$ factor is valid as far as the assumptions σ_a and $\exp(-\rho\sigma_s t)$ are satisfied. Water with 0.2 mm thick and thinner satisfies this criterion. However, it does not work for a scatterer having a considerable absorption cross-section, e.g., vanadium. On the other hand, the proposed method in this work is applicable to such a scatter since the effects of multiple scattering and absorption are separately considered.

2.5 Conclusion

A new method to evaluate the incoherent scattering intensity is proposed. By re-visiting the theoretical treatment of multiple scattering followed by carefully analyzing the sample–thickness dependence and hydrogen–number density dependence of

the incoherent scattering intensity for low–density polyethylene and mixtures of light and heavy water, the following relationship was derived. The scattering intensity is given by

$$\frac{\mathrm{d}\Sigma}{\mathrm{d}\Omega} \approx \left\langle \frac{\mathrm{d}\Sigma}{\mathrm{d}\Omega} \right\rangle_0 \frac{e^{Kt} - 1}{Kt},$$

with

$$K = \sum_{\mathrm{i}} \rho_{\mathrm{i}} \sigma_{\mathrm{s,i}},$$
$$\left\langle \frac{\mathrm{d}\Sigma}{\mathrm{d}\Omega} \right\rangle_0 = \frac{K}{4\pi}.$$

Here, $\langle(\mathrm{d}\Sigma/\mathrm{d}\Omega)\rangle_0$ is the differential scattering cross-section at single-scattering limit and $(e^{Kt} - 1)/Kt$ is the correction term. This equation was examined for hydrogen-rich systems, i.e., low–density polyethylene and for systems where the hydrogen number density varies in the wide range, i.e., light and heavy water mixtures. The linear attenuation coefficient, μ (equivalent to the sum of the product of the number–density of atoms and total cross-section of component i to all the component in the system) for H_2O and D_2O mixtures are given by

$$\mu = (\mu_{\mathrm{H}} - \mu_{\mathrm{D}}) f_{\mathrm{H}} + \mu_{\mathrm{D}},$$

with $\mu_{\mathrm{H}} = 6.22\ \mathrm{cm}^{-1}$ and $\mu_{\mathrm{D}} = 0.588\ \mathrm{cm}^{-1}$, where μ_{H} and μ_{D} are the linear attenuation coefficient of H_2O and D_2O, respectively. Application to a polymer solution also supports the validity of the proposed equation. The scattering from water is also approximately given by the following equation,

$$\left\langle \frac{\mathrm{d}\Sigma}{\mathrm{d}\Omega_{\mathrm{H_2O}}}(q) \right\rangle = 0.689 \frac{\exp[5.40t] - 1}{5.40t} [\mathrm{cm}^{-1}],$$

at least up to $t = 0.4$ cm. Although a significant disagreement is found in the observed and theoretical values of $\langle(\mathrm{d}\Sigma/\mathrm{d}\Omega)_{\mathrm{inc}}(q)\rangle_0$ for H_2O, which is mainly due to inelastic scattering from water, it is now available to predict the incoherent scattering intensity of hydrogen–containing materials with reasonable accuracy with the correction factor proposed in this chapter.

References

[1] Schelten, J.; Schmatz, W. *J. Appl. Cryst.* 1980, **13**, 385.

[2] Jacrot, B. *Rep. Prog. Phys.* 1976, **39**, 911.

[3] May, R.P.; Ibel, K.; Haas, J. *J. Appl. Cryst.* 1982, **15**, 15.

[4] Wignall, G.D.; Bates, F.S. *J. Appl. Cryst.* 1987, **20**, 28.

[5] Dubner, W.S.; Schultz, J.M.; Wignall, G.D. *J. Appl. Cryst.* 1990, **23**, 469.

[6] Maconnachie, A. *Polymer* 1984, **25**, 1068.

[7] Carsughi, F.; May, R.P.; Plenteda, R.; Saroun, J. *J. Appl. Cryst.* 2000,**33**, 112.

[8] Stothary, P.H. *J. Appl. Cryst.* 1987, **20**, 362.

[9] Lindner, P. *J. Appl. Cryst.* 2000, **33**, 807.

[10] Lindner, P.; Leclercq, F.; Damay, P. *Physica B* 2000, **291**, 152.

[11] Sears, V.F. *Neutron News* 1992, **3**, 29.

[12] Brockhouse, B.N. *Phys. Rev.* 1955 **95**, 1721.

[13] Schwahn, D.; Takeno, H.; Willner, L.; Hasegawa, H.; Jinnai, H.; Hashimoto, T.; Imai, M. *Phys. Rev. Lett.* 1994, **73**, 3427.

[14] Glinka, C. *National Institute of Standards and Technology Center for Neutron Research, SANS Data Reduction and Imaging Software* 1999, **25**.

[15] Shibayama, M.; Isono, K.; Okabe, S.; Karino, T.; Nagao, M. *Macromolecules* 2004, **37**, 2909.